iScience

Article

Global transcriptional changes across multiple isogenic *C9orf72* patient iPSC-derived neurons

Graphical abstract

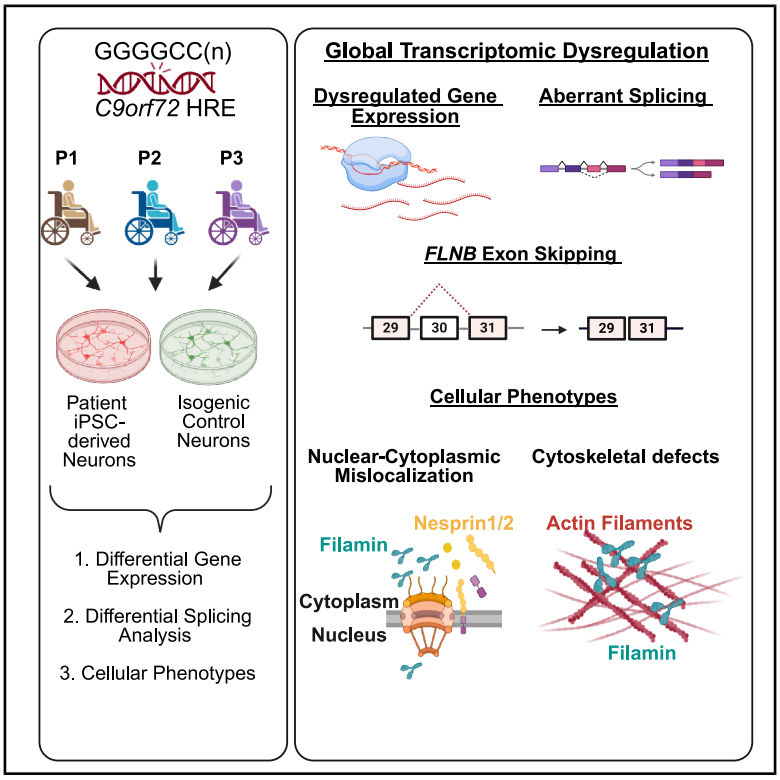

Highlights

- RNA-seq of isogenic *C9orf72* iPSC neurons reveals robust transcriptomic changes
- Cytoskeletal, ECM and synaptic pathways are consistently dysregulated
- *FLNB* shows exon 30 skipping across multiple *C9orf72* iCN lines
- Altered FLNB localization and cytoskeletal defects observed in *C9orf72* iCNs

Authors

Aparna Sreeram, Desiree M. Baron, Alberto Brusati, Karly Stallworth, Jack Humphrey, John E. Landers

Correspondence

john.landers@umassmed.edu

In brief

Genomics; Neuroscience; Cell biology

Sreeram et al., 2026, iScience *29*, 116054
June 19, 2026 © 2026 Published by Elsevier Inc.
https://doi.org/10.1016/j.isci.2026.116054

CellPress

iScience

CellPress
OPEN ACCESS

Article

Global transcriptional changes across multiple isogenic *C9orf72* patient iPSC-derived neurons

Aparna Sreeram,[1,2] Desiree M. Baron,[1] Alberto Brusati,[1] Karly Stallworth,[1] Jack Humphrey,[3,4,5,6] and John E. Landers[1,7,*]
[1]Department of Neurology, University of Massachusetts Chan Medical School, Worcester, MA 01605, USA
[2]Program in Neuroscience, Graduate School of Biomedical Sciences, University of Massachusetts Chan Medical School, Worcester, MA 01605, USA
[3]Department of Neuroscience, Icahn School of Medicine at Mount Sinai, New York, NY, USA
[4]Department of Genetics and Genomic Sciences, Icahn School of Medicine at Mount Sinai, New York, NY, USA
[5]Ronald M. Loeb Center for Alzheimer's Disease, Icahn School of Medicine at Mount Sinai, New York, NY, USA
[6]Estelle and Daniel Maggin Department of Neurology, Icahn School of Medicine at Mount Sinai, New York, NY, USA
[7]Lead contact
*Correspondence: john.landers@umassmed.edu
https://doi.org/10.1016/j.isci.2026.116054

SUMMARY

Hexanucleotide repeat expansions in *C9orf72* are the most common genetic cause of amyotrophic lateral sclerosis (ALS) and frontotemporal degeneration (FTD); yet, mechanisms underlying selective neuronal vulnerability remain unclear. A major challenge in identifying consistent transcriptomic changes across *C9orf72* patient-derived neuron lines has been heterogeneous differentiations, lack of isogenic controls and low sequencing depth. To overcome these challenges, we generated homogeneous cortical neuron (iCNs) cultures from multiple isogenic *C9orf72* patient iPSC pairs and performed RNA deep sequencing. We identified robust and reproducible gene expression and splicing alterations in pathways related to cytoskeletal organization, extracellular matrix adhesion and synaptic signaling. Notably, we observed exon 30 skipping in the cytoskeletal regulator filamin B (*FLNB*), resulting in loss of its hinge domain. This was accompanied by altered FLNB localization, disrupted actin crosslinking, and mechanotransduction signaling. These findings reveal convergent transcriptomic and functional disruptions across multiple isogenic *C9orf72* patient-derived iCNs offering insights into ALS/FTD pathogenesis.

INTRODUCTION

Amyotrophic lateral sclerosis (ALS) and frontotemporal dementia (FTD) are fatal neurodegenerative disorders with overlapping clinical, pathological and genetic features.[1] The most common genetic cause of both diseases is a GGGGCC hexanucleotide repeat expansion (HRE) in a non-coding region of the *chromosome 9 open reading frame 72* (*C9orf72*) gene, accounting for ~40% of familial ALS, ~25% of familial FTD, and 2%–7% of sporadic ALS/FTD cases.[2–5] This large intronic expansion is thought to drive disease pathogenesis through three non-mutually exclusive mechanisms: (1) loss of function via *C9orf72* haploinsufficiency; (2) RNA toxicity from sense and antisense repeat transcripts; and (3) production of toxic dipeptide repeat proteins (DPRs) via repeat-associated non-AUG (RAN) translation. These pathways converge to disrupt fundamental cellular processes, including nucleocytoplasmic transport, RNA processing, proteostasis, and cytoskeletal dynamics.[6–14] However, the precise molecular drivers of *C9orf72*-associated ALS remain unclear due to the complexity of these intersecting pathways. This makes it challenging to define the early, neuron-intrinsic, and convergent molecular changes underlying selective neuron vulnerability. Identifying such early events is critical for advancing therapeutic target discovery and biomarker development.

Human induced pluripotent stem cell (iPSC)-derived neurons offer a powerful model to investigate early, cell-autonomous mechanisms underlying ALS/FTD. When coupled with global transcriptomic profiling, this system enables an unbiased and comprehensive analysis of gene expression and splicing changes, capturing reproducible, neuron-specific alterations across genetically diverse patient lines. This strategy provides critical insights into early molecular drivers of disease pathogenesis and helps to identify potential therapeutic targets and biomarkers. However, achieving consistent, transcriptomic signatures across *C9orf72* patient neurons has been limited by several factors. Neuronal cultures derived from *C9orf72* isogenic iPSCs lines are often heterogeneous due to variability in differentiation protocols resulting in inconsistent results and difficulties in deciphering changes in transcriptional signals from bulk RNA sequencing approaches. Comparisons of mutant lines must overcome inherit differences in genetic background which can mask identification of transcriptional differences directly resulting from the repeat expansion. Further, accurate identification of altered splicing events and differentially expressed rare transcripts becomes challenging as signal gets diluted from mixed cell population and can obscure subtle; yet, biologically relevant changes associated with the *C9orf72* repeat expansion.

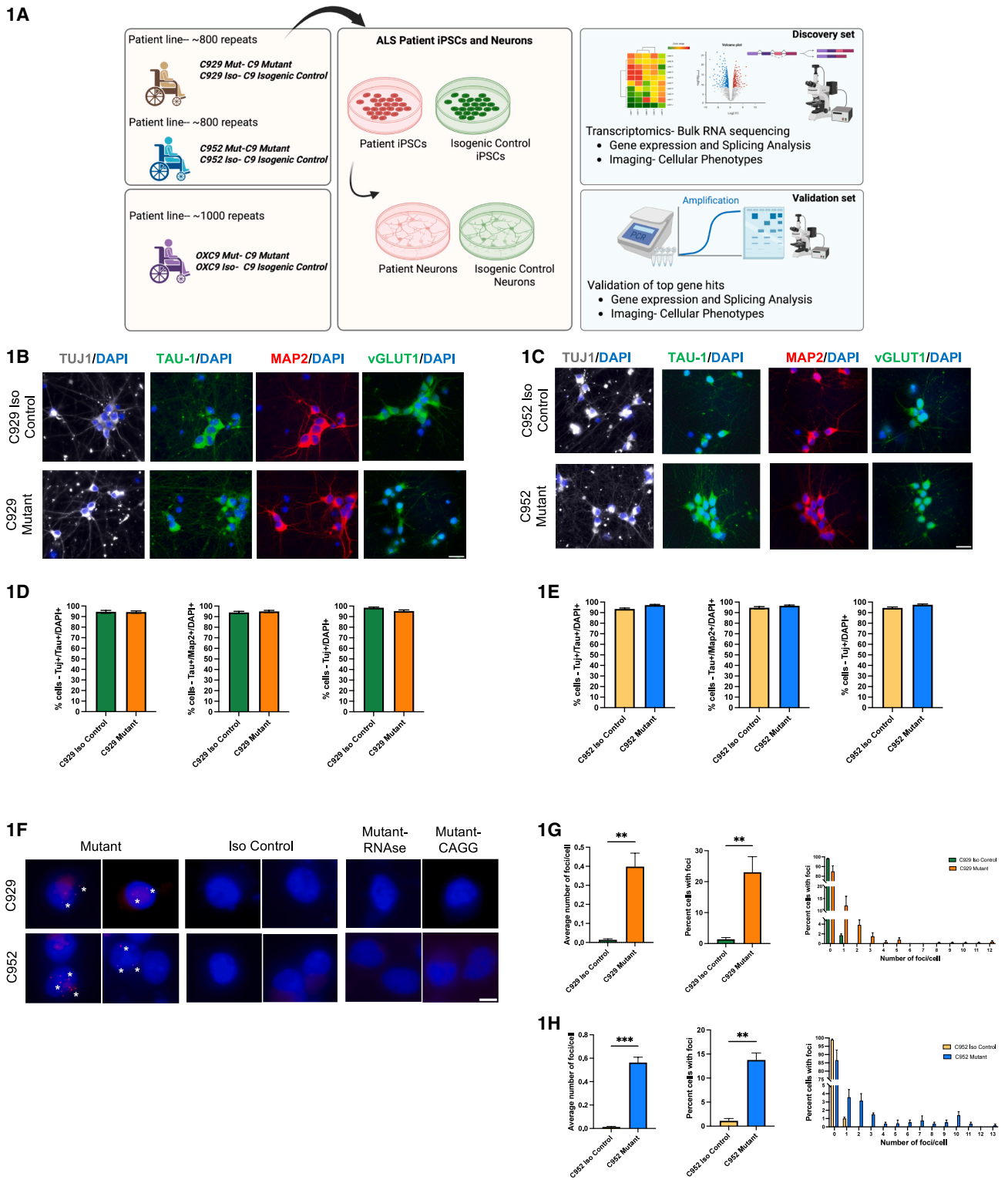

Figure 1. Differentiation and characterization of *C9orf72* iPSC-iCNs

(A) Schematic overview of the study design showing *C9orf72* isogenic iPSC lines and key methodologies used. Figure created in https://BioRender.com.

(B and C) Representative immunofluorescence images of neuronal markers Tuj1, Tau-1, MAP2, and vGLUT1 at DIV15 for C929 and C952 iCN lines. Scale bars, 20 μm.

(legend continued on next page)

To overcome these challenges and to increase rigor, we established an experimental framework using three patient-derived *C9orf72* iPSC lines and their CRISPR-Cas9-corrected controls, forming a comprehensive collection of isogenic system for this genotype. To overcome the limitations of heterogeneous neuronal cultures, iPSC lines were differentiated into highly pure populations (>90%) of cortical neurons (iCNs) using a neurogenin-2 (NGN2) transcription factor-mediated method.[15] Lastly, we have incorporated high depth RNA sequencing to facilitate the identification of reproducible altered splicing events and differentially expressed rare transcripts.

Our transcriptomic analysis revealed robust and reproducible dysregulation of gene expression and splicing in cellular pathways involved in cytoskeletal organization, extracellular matrix (ECM) adhesion and synaptic signaling. We identified a core set of genes within these pathways that were consistently altered in their expression across multiple *C9orf72* iCN isogenic pairs. Notably, we uncovered a reproducible exon-skipping event in the cytoskeletal regulator filamin B (*FLNB*), which was accompanied by corresponding cellular defects, including FLNB nuclear clearance, altered actin crosslinking, and dysregulation of mechanotransduction signaling. Together, our study provides a convergent transcriptomic and mechanistic insight into early pathogenic processes across multiple isogenic *C9orf72* patient-derived iCNs and offers new understanding of ALS/FTD pathogenesis.

RESULTS

Patient derived *C9orf72* iPSCs yield high purity iCNs that stain for G4C2 RNA foci early during differentiation.

To perform our study, we selected two previously well-characterized *C9orf72* patient-derived iPSC lines with ~800 repeats (C929 mutant and C952 mutant) and their corresponding isogenic controls (C929 Iso control and C952 Iso control) to use for the discovery of altered transcripts by RNA sequencing (RNA-seq).[16] Further, we validated our study findings in a third previously established isogenic pair, OXC9 mutant and OXC9 Iso control, derived from a patient with ~1,000 repeats.[17] The workflow of the study design is as represented in Figure 1A. All three sets of iPSC lines stained positive for pluripotent markers Oct3/4 and Sox2 (Figures S1A, S1D, and S1G) showed normal karyotyping as determined by the G-band karyotyping (Figures S1B, S1E, and S1H). Lastly, all mutant and isogenic iPSC lines displayed proper concordance for *C9orf72* repeat expansions (Figures S1C, S1F, and S1I).

To generate a homogeneous population of cortical neurons, all iPSC lines were differentiated via NGN2-directed programming, yielding cultures composed of >90% iCNs. Neuronal identity was validated by the expression of canonical markers, including Tuj1, MAP2, Tau-1, and vGLUT1 (Figures 1B–1E). Importantly, no major differences in neuronal marker expression were observed between isogenic controls and *C9orf72* mutant lines. This approach resulted in substantially higher purity compared to conventional chemical differentiation protocols (~30%–40%).

Expanded *C9orf72* G4C2 repeats are known to produce nuclear RNA foci, a pathological hallmark of *C9orf72*-associated ALS/FTD.[8,18] Consistent with this, we detected an increased level of sense RNA foci in both C929 and C952 mutant iCNs compared to their isogenic controls (Figures 1F–1H). The presence of RNA foci at DIV15 confirms that the pathogenic repeat expansion is retained in our iCN models and that disease-associated molecular alterations emerge early during neuronal differentiation.

C9orf72 iCNs differentially express genes enriched in ALS-relevant cellular pathways

Bulk RNA-seq-based lineage marker analysis confirmed that NGN2-induced neuronal cultures exhibit a predominantly cortical-like excitatory neuronal identity, with robust and consistent expression of neuronal markers (*TUBB3*, *NEFL*, *STMN2*, *PRPH*, *MAP2*, *SYP*, *SNAP25*, *DLG4*, *SLC17A6/vGLUT2*, *SYN1*, *RBFOX3/NeuN*, and *SLC17A7/vGLUT1*) and minimal expression of pluripotency/progenitor or glial markers (Figure S5A). Importantly, this expression pattern was highly reproducible across biological replicates within each line and comparable between isogenic control and *C9orf72* mutant neurons, indicating minimal intra-line variability and no systematic differences in lineage composition between genotypes.

To investigate global gene expression changes associated with *C9orf72* ALS, we performed bulk RNA deep sequencing on our discovery cohort (C929 mutant and Iso control, C952 mutant and Iso control) from iCNs collected at DIV15 of neuronal differentiation. To facilitate the identification of reproducible altered splicing events and differentially expressed rare transcripts, RNA-seq was performed at high depth (100M paired-end reads, 2 × 150 bp) from three independent batch differentiations per line. RNA-seq analysis revealed 2,388 total differentially expressed genes (DEGs) of which 1,912 were protein-coding in C929 mutant iCN line compared to its isogenic line, while C952 mutant iCNs showed 699 DEGs and 550 protein-coding DEGs relative to its isogenic control (p adj<0.05, $|Log_2FC|$ >0.35, n = 3 biological replicate per line) (Figure 2A; Table S1). To gain insight into the biological impact of these expression changes, we subjected the protein coding DEGs (p adj< 0.05, $|Log_2FC|$ >0.35) from each line to pathway enrichment analysis using Metascape, which integrates Gene ontology, KEGG, and other curated pathway databases. Across both patient lines, significantly dysregulated genes were enriched in three major neuronal biological processes: cytoskeletal

(D and E) Quantification of the percentage of Tuj1, Tau-1, and MAP2-positive cells in C929 and C952 isogenic control and mutant iCNs at DIV15. n = 3 biological replicates per line; ~500–600 cells per line.

(F) Representative RNA FISH images showing Cy3-labeled sense repeat RNA foci in C929 and C952 mutant iCNs at DIV15. Arrows indicate RNA foci. Scale bars, 5 μm.

(G and H) Quantification of RNA foci in C929 and C952 mutant iCNs, including average number of foci per cell, percentage of cells with foci, and distribution of foci per cell. n = 3 biological replicates per line; ~500 cells for C929 and ~350–400 cells for C952.

Data in (D, E, G, and H) are shown as mean ± SEM. Statistical analysis by unpaired two-tailed t test. $p < 0.05$ (*), $p < 0.01$ (**), $p < 0.001$ (***), and $p < 0.0001$ (****).

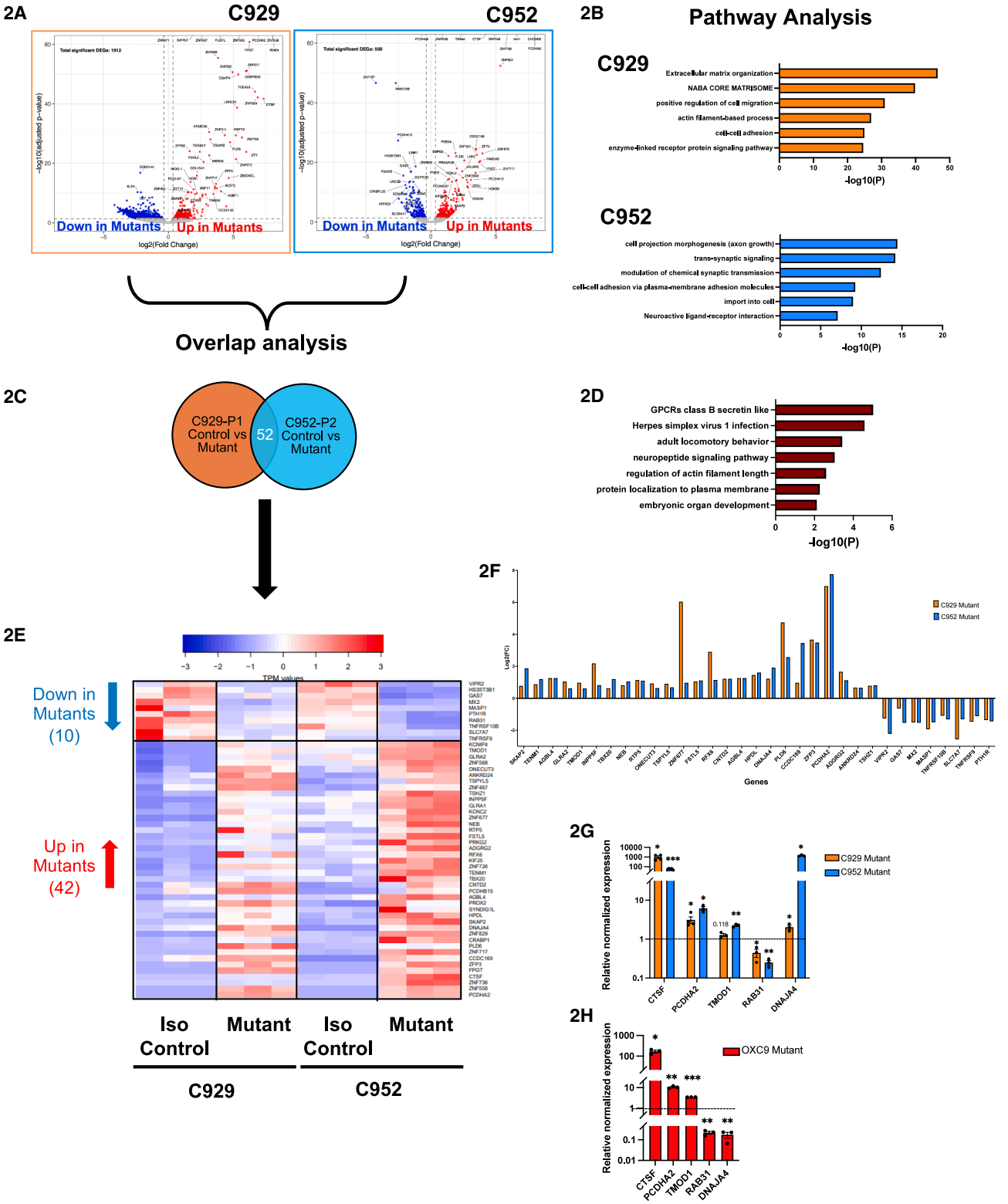

Figure 2. Transcriptomic analysis reveals robust and overlapping gene expression changes across multiple *C9orf72* isogenic iCNs

(A) Volcano plots showing top differentially expressed protein coding genes in C929 and C952 mutant iCNs vs. their isogenic controls. $n = 3$ biological replicates per line; Wald test; p adj<0.05, $|\text{Log}_2\text{FC}| > 0.35$. Genes represented in blue are downregulated in mutants and red are upregulated in mutants. Significant genes are indicated on the top of the plot; C929, 1,912 genes and C952, 550 genes.

(legend continued on next page)

organization, synaptic function, and cell adhesion/ECM remodeling (Figures 2B, S2A, and S2B).

Given the enrichment of similar gene pathways across both patient lines, we next examined whether any overlapping gene expression changes were present. Correlation and overlap analysis of all DEGs between the C929 and C952 iCN lines revealed shared transcriptional alterations. Scatterplot analysis of $\log_2$fold-change values for genes significant in either dataset showed a modest positive correlation (Pearson r = 0.17), indicating partial concordance in expression changes across lines. A total of 124 genes overlapped between the datasets, including 75 with concordant directionality (Figures S2C and S2E). Hypergeometric testing demonstrated that this overlap was significantly higher than expected by chance (expected = 29 genes; observed = 124 genes; $p = 2.1 \times 10^{-42}$), suggesting that a subset of genes consistently altered across independent patient-derived iCN lines (Figure S2D). These findings further indicate that while both lines affect similar biological pathways, the specific genes perturbed differ across patients, likely reflecting inter-patient variability or cell line-specific transcriptional heterogeneity commonly observed in iPSC-based ALS models. Differential expression analysis further identified 52 of these 75 concordant DEGs as protein coding, with 42 upregulated and ten downregulated relative to their respective isogenic controls (Figures 2C–2E). As expected, pathway enrichment analysis of these overlapping DEGs revealed significant dysregulation in cytoskeletal organization, synaptic signaling and cell adhesion/motility. These pathways are broadly implicated in ALS/FTD pathogenesis highlighting convergent molecular signatures across patient lines (Figure 2D). Further analysis of the common DEGs revealed that 33 of those genes were involved in mechanosensory pathways, cellular migration and movement, processes which are fundamentally mediated by cytoskeletal dynamics and cell adhesion. Dysregulation of these components may therefore represent a key mechanism contributing to disease-relevant neuronal dysfunction (Figure 2F).

To further validate the robustness of our transcriptomic findings in the *C9orf72* patient-derived neurons, we selected five genes for quantitative real-time PCR (qPCR) validation. Candidate genes were chosen based on three criteria: (1) consistent differential expression across three biological replicates in both C929 and C952 lines, (2) ~1.5- to 2-fold changes in expression across both lines, and (3) known involvement in ALS pathophysiology or relevance to key pathways identified in our earlier enrichment analyses. TaqMan qPCR confirmed the RNA-seq results for *CTSF* (cathepsin F), *PCDHA2* (protocadherin alpha 2), *RAB31* (RAS oncogene family member), and *DNAJA4* (DnaJ heat shock protein family member A4) across both mutant lines relative to their respective isogenic controls. *TMOD1* (tropomodulin 1) showed significant expression changes in C952 mutant line and a consistent, though not statistically significant, trend in the C929 mutant line, each compared with their respective isogenic controls (Figure 2G). Notably, *DNAJA4* expression was markedly higher in C952 mutant iCNs compared to C929 iCNs, suggesting potential line-specific differences in the magnitude of stress-response pathway activation.

To further assess the reproducibility of our transcriptomic findings, we extended our validation to a third isogenic pair of iCNs (OXC9 mutant, OXC9 Iso control). qPCR analysis revealed consistent expression patterns for the selected genes across this additional *C9orf72* iCN pair (Figure 2H). A notable exception was *DNAJA4*, which exhibited reduced expression in the OXC9 mutant line, contrasting with the upregulation observed in C929 and C952 mutant iCNs. This variability suggests that *DNAJA4* dysregulation may be context- or line-dependent, rather than a uniform feature of *C9orf72* mutant neurons.

Taken together, these results indicate that *CTSF*, *PCDHA2*, *TMOD1*, and *RAB31* may serve as molecular transcriptional alterations across multiple independent *C9orf72* iPSC-derived neuronal models. Their consistent dysregulation across multiple patient lines shows their potential relevance to early-stage disease mechanisms and possibly be promising candidates for further investigation as biomarkers of ALS progression.

While *DNAJA4* emerges as a responsive gene across the *C9orf72* lines, its variable directionality across patient lines suggests that it may reflect secondary or stress-associated responses rather than a direct disease signature. Accordingly, *DNAJA4* is considered here as a candidate gene warranting further investigation, whereas the other genes represent more robust early-stage transcriptional alterations associated with *C9orf72* mutant neurons.

Among the differentially expressed genes, cathepsin F (*CTSF*), a lysosomal protease involved in autophagy and apoptotic priming was significantly upregulated across all three *C9orf72* patient iCN lines. Given the established role of autophagic and apoptotic dysregulation in *C9orf72*-ALS,[19] we assessed CTSF protein levels in C929 iCN line. Immunostaining revealed a predominant and increased nuclear accumulation of CTSF in mutant iCNs compared to isogenic controls (Figures S2F and S2G). This nuclear enrichment may reflect cellular stress or senescence, both linked to ALS-related neuronal dysfunction. As *C9orf72* mutant neurons have previously been shown to have vulnerability

(B) Pathway enrichment analysis of differentially expressed genes in C929 and C952 mutant iCNs.
(C) Venn diagram showing overlap of concordantly regulated genes between C929 and C952 mutants.
(D) Pathway enrichment analysis of 52 overlapping, concordantly regulated genes.
(E) Heatmap of the 52 overlapping differentially expressed genes in C929 and C952 mutant iCNs vs. their controls.
(F) Bar graph depicting overlapping differentially expressed genes in mechanotransduction, cell movement, and migration pathways in C929 and C952 mutant iCNs normalized to their respective isogenic controls. $n = 3$ biological replicates per line.
(G) Validation of selected genes using TaqMan qPCR in C929 and C952 mutant iCNs, normalized to their respective isogenic controls. The dotted line indicates the normalized control value. $n = 3$–5 biological replicates per line.
(H) TaqMan qPCR validation of top differentially expressed genes in OXC9 mutant iCNs, normalized to the isogenic control. The dotted line indicates the normalized control value. $n = 3$ biological replicates.
Data in (G and H) represent mean ± SEM. Statistical analysis by unpaired two-tailed *t* test with Welch's correction. $p < 0.05$ (*), $p < 0.01$ (**), $p < 0.001$ (***), and $p < 0.0001$ (****).

under stress conditions such as nutrient deprivation and excitotoxicity,[19–21] we next evaluated whether increased CTSF was associated with ongoing apoptosis. Western blot analysis of cleaved caspase-3, a marker of late-stage apoptosis, revealed no changes in protein levels between mutant and isogenic neurons at DIV15 (Figures S2H and S2I). These findings at early timepoints suggest that *C9orf72* iCNs may be in a primed or pre-apoptotic state and that CTSF upregulation may serve as an early marker of neuronal dysfunction preceding overt cell death.

C9orf72 iCNs show splicing aberrations in genes belonging to ALS-relevant cellular pathways

Given our transcriptomic analysis revealed widespread gene expression alterations in *C9orf72* iPSC-derived neurons, we next aimed to determine whether these changes could, in part, be driven by disruptions in RNA splicing. Moreover, *C9orf72* repeat expansions have been previously associated with RNA-binding protein sequestration and the formation of RNA foci, both of which could perturb the normal splicing machinery.[16,21,22] Thus, we hypothesized that changes in splicing could represent an additional regulatory layer underlying the transcriptional alterations observed in our dataset.

To investigate the global splicing alterations associated with *C9orf72* ALS, we performed a comprehensive splicing analysis of C929 and C952 iCN lines using rMATS (replicate multivariate analysis of transcript splicing).[23] In the C929 mutant line, we identified 1,286 splicing events compared to its isogenic control, whereas the C952 mutant line exhibited 235 aberrant splicing events relative to its respective control (FDR <0.15; percent spliced in $|\Delta PSI| \geq 0.2$). Most of these splicing alterations were cassette exons (SE), accounting for 87% in C929 and 75% in C952, followed by alternative 5′ splice sites (A5′SS-5.6% and 5%, respectively), alternative 3′ splice sites (A3′SS-4% and 8%, respectively), retained introns (RI-3% and 10%, respectively), and mutually exclusive exons (MXE-0.4% and 2%, respectively) (Figure 3A; Table S2). When the splicing events were further examined for overlap at the same exon-junction level across the two lines, we identified 15 genes commonly affected. Among these, 12 genes exhibited SE, two genes showed RI, and two gene displayed an A3′SS (Figure 3B).

To assess the biological significance of these splicing alterations, we performed pathway enrichment analysis of all significant splicing events (FDR <0.15; $|\Delta PSI| \geq 0.2$) using Metascape. Both C929 and C952 mutant lines revealed enrichment of highly overlapping pathways, including cytoskeletal organization, ECM adhesion, synaptic and intracellular trafficking processes (Figures 3C, 3D, S3A, and S3B). While the C929 line showed strong enrichment in cytoskeletal regulation, cell-matrix adhesion and synaptic/membrane trafficking, the C952 line highlighted pathways reflecting perturbations in microtubule-based processes along with intracellular transport, cytoskeleton-mediated remodeling and synaptic signaling. These results indicate that, despite differences in the overall number of splicing events, both lines converge on similar biological networks critical for neuronal cytoskeleton, maintenance and communication. The recurrence of cytoskeletal, adhesion and trafficking pathways across both gene expression and splicing analyses suggests coordinated disruption of these processes in *C9orf72* mutant neurons. Further, since our datasets showed most of the splicing alterations from cassette exons, we decided to further investigate into the specific genes altered. The volcano plots for differential splicing analysis for cassette exons are depicted in Figure 3E and the remaining splicing alterations observed are depicted in Figures S3C and S3D (FDR<0.15; $|\Delta PSI| \geq 0.2$ are labeled). To further investigate which RBPs may contribute to the observed cassette exon changes, we applied rMAPS2,[24] which assesses position-dependent enrichment of RBP binding motifs in differentially spliced genes. This analysis revealed significant enrichment of binding motifs for several RBPs implicated in neurological disease, including SRSF1, HNRNPK, and FMR1, with strong enrichment observed in upstream intronic regions, among others, across both lines (Figure S3E). Although these findings implicate dysregulated RBP activity in splicing alterations, the precise mechanisms by which these RBPs influence RNA processing and downstream pathways in *C9orf72* iCNs remain to be determined.

Bulk RNA sequencing identifies exon 30 skipping in filamin B in *C9orf72* iCNs

Among the notable overlapping cytoskeletal genes affected by alternative splicing, *FLNB* emerged as one of the key targets, in our transcriptomic analysis, exhibiting a consistent exon 30 skipping event in both C929 and C952 mutant iCN lines (Figure 3B). Figure 4A shows exon 30 with its flanking exon structure and the corresponding exon-skipping event and protein domains encoded, while Figure 4B illustrates all the FLNB protein domains. FLNB encodes an actin-binding protein characterized by a conserved N-terminal actin-binding domain, two hinge regions, and 24 immunoglobulin-like (Ig-like) repeat domains and a C-terminal dimerization domain.[25–28] Functionally, FLNB plays a central role in cytoskeletal architecture through actin bundling and crosslinking and nuclear gene transcriptional regulation, with secondary role in mechanosensory and cell migration signaling by linking the cytoskeleton to the ECM.[25,29,30–34] Exon 30 specifically encodes the first hinge (H1) domain, which is critical for maintaining protein flexibility during actin crosslinking and further contains a cleavage site within this domain that is important for translocation of filamin into the nucleus for its gene transcription and regulatory functions.[30] *FLNB* exon 30 is a (24aa) exon, therefore skipping of this exon leads to an in-frame deletion of the exon 30, resulting in the loss of the H1 domain, without altering the remainder of the protein. To visualize the *FLNB* exon-skipping event, we examined its splicing patterns using Sashimi plots generated from Integrative Genomics Viewer (IGV). These plots revealed a clear reduction in read coverage across exon 30 and increased splice junction reads connecting exons 29 and 31 in both C929 and C952 mutant neurons compared with their respective isogenic controls, consistent with exon 30 skipping (Figures 4C and 4D).

To validate the *FLNB* splicing alteration, we performed RT-PCR and droplet digital PCR (ddPCR) on C929 and C952 iCNs. The analysis revealed a decrease in the mean percent spliced-in (PSI) value for exon 30 in the mutant lines compared with their isogenic controls, indicating increased skipping of exon 30 in the mutant iCNs (Figures 4E and 4F) To validate our findings on an additional patient iCNs, we extended this

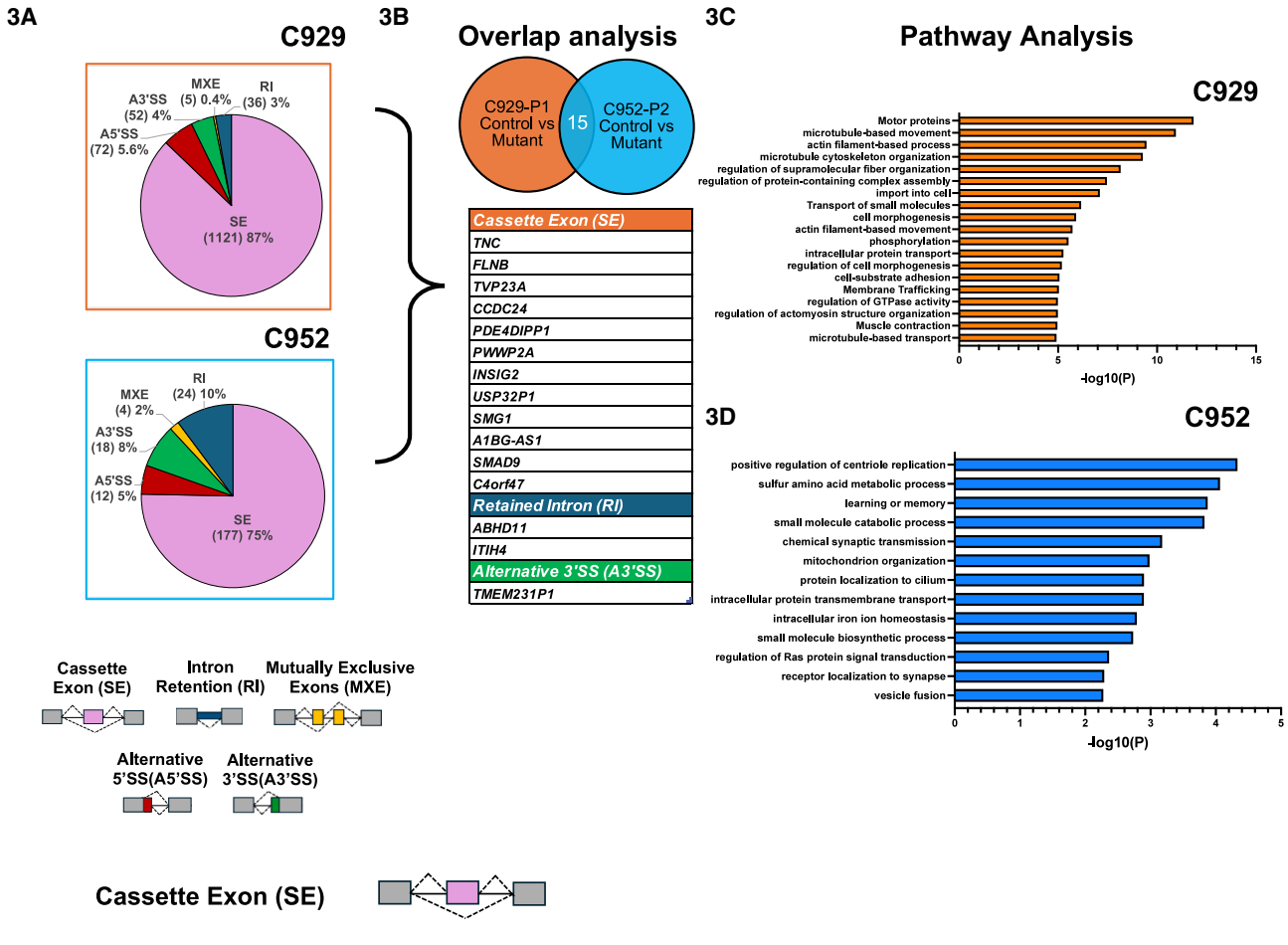

Figure 3. Widespread splicing alterations in *C9orf72* mutant iCNs converge on cytoskeletal and signaling pathways

(A) Pie chart showing the distribution of differential splicing event types in C929 and C952 mutant iCNs identified from RNA-seq data. The number of events for each category is indicated in parentheses. $n = 3$ biological replicates per line. Events were defined by $|\Delta PSI| \geq 0.2$ and FDR < 0.15. Categories include cassette exons (SE), intron retention (RI), MXEs, and alternative 5′ or 3′ splice sites (A5′/A3′SS).

(B) Overlap analysis showing 15 genes with common splice site alterations across both C929 and C952 mutant lines.

(C and D) Pathway enrichment analysis of differentially spliced genes affected by all splicing event types, highlighting commonly altered cytoskeletal and signaling pathways in both lines.

(E) Volcano plot of cassette exon splicing changes, top most significant genes with $|\Delta PSI| \geq 0.2$, FDR < 0.15 are labeled. FLNB is highlighted by a circle.

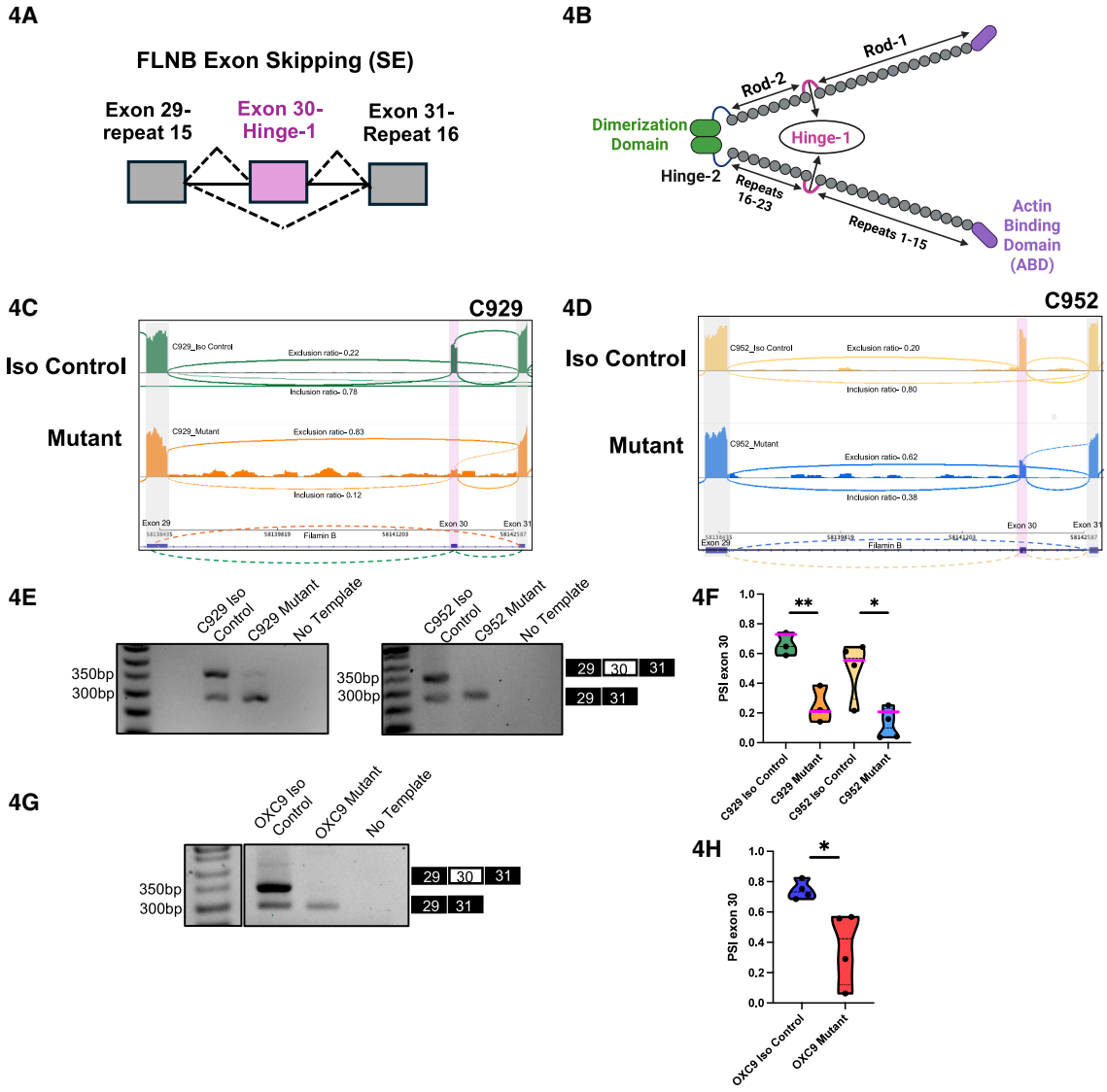

Figure 4. *C9orf72* mutant iCNs exhibit increased exon 30 skipping in the *FLNB* gene

(A) Schematic illustrating the *FLNB* exon 30 with its flanking exons and annotated protein domains and their respective exon boundaries indicated by (B) FLNB protein structure. The Hinge-1 domain is highlighted by a circle.

Figure created in https://BioRender.com.

(C and D) Sashimi plots showing exon 30 skipping between exons 29 and 31 of *FLNB* in C929 and C952 mutant iCNs compared with their isogenic controls.

(E–G) Experimental validation of *FLNB* exon 30 splicing in C929 and C952 mutant iCNs.

(E) RT-PCR analysis and (F) quantification of exon 30 percent spliced-in (PSI) by ddPCR. RNA-seq based of mean PSI quantification is indicated by the magenta line.

(G) RT-PCR validation and (H) ddPCR quantification of exon 30 PSI in OXC9 iCNs.

Data in (F and H) are shown as mean ± SEM ($n = 3$–4 biological replicates per line). Statistical analysis was performed using two-way ANOVA with Sidak's multiple comparisons test. $p < 0.05$ (*), $p < 0.01$ (**), $p < 0.001$ (***), and $p < 0.0001$ (****).

analysis to the OXC9 lines. Interestingly, the OXC9 mutant line also demonstrated a similar decrease in PSI exon 30, consistent with the C929 and C952 mutant iCN lines (Figures 4G and 4H). This shows the consistent splicing alterations in *FLNB* across the three *C9orf72* patient lines relative to their isogenic controls.

To further explore whether this splicing event is neuron-specific, we examined *FLNB* splicing in *C9orf72* patient-derived fibroblast lines compared to healthy controls. No significant PSI exon 30 changes were observed (Figures S4A and S4B) suggesting that the *FLNB* exon 30 skipping event may be neuron-specific or may be influenced by cell-type specific splicing regulation. This *FLNB* skipping event highlights the potential role of alternative splicing in contributing to cytoskeletal dysfunction in *C9orf72* ALS. These findings emphasize the

importance of investigating splicing changes in the context of patient-derived iPSC lines, as they may offer critical insights into the molecular mechanisms driving ALS pathology and identify therapeutic targets for intervention.

Exon 30 skipping in *FLNB* disrupts nuclear localization, alters actin crosslinking and impairs mechanotransduction in *C9orf72* iCNs

FLNB plays critical roles in neurite outgrowth, actin crosslinking/bundling and mechanosensory signaling.[26,29,35,36] In addition to these cytoplasmic functions, FLNB also localizes and plays critical roles in the nucleus, where it regulates gene transcription of several cell adhesion/DNA damage response/cytoskeletal genes.[32–34] Previous reports have shown that exon 30 hinge domain skipping affects FLNB nuclear localization and impairs their ability to provide flexibility to actin networks to withstand mechanical stresses.[36,37] Further, nuclear-cytoplasmic transport defects have been well established in *C9orf72*-ALS.[11,21,38] Based on this information, we examined FLNB subcellular distribution in *C9orf72* mutant iCNs. Immunostaining revealed a cellular redistribution of FLNB from the nucleus to the cytoplasm, particularly around the soma in C929 and C952 mutant iCN lines compared to their isogenic controls (Figures 5A–5D). These findings suggest that exon 30 skipping may possibly impair nuclear import of FLNB, resulting in its cytoplasmic accumulation. Since FLNB mislocalization suggested a possible impairment in its nuclear import, we next asked whether this phenomenon reflected a more general disruption of nuclear-cytoplasmic transport as reported previously.[21] To address this, we examined the localization of Ran, a key nuclear transport factor, and TDP-43, an RNA-binding protein previously reported to be mislocalized in *C9orf72* neurons.[11,21,39–41] While TDP-43 remained largely nuclear in C929 mutant iCNs (Figures S4C and S4D), C929 iCNs showed that Ran exhibited an increase in cytoplasmic localization in mutant iCNs (Figures S4E and S4F), indicating a potential global nuclear transport defects that may also contribute to FLNB mislocalization in the mutants in addition to the FLNB exon 30 skipping events.

Given FLNB's role in actin crosslinking,[30] we investigated whether actin network organization was altered in *C9orf72* mutant iCNs. Phalloidin staining revealed increased actin filament density in mutant iCNs relative to its isogenic controls (Figures 5E and 5F). We hypothesized that this increase in actin density could possibly result from FLNB's cellular redistribution along the neurites. Co-localization analysis showed enhanced FLNB distribution along neurites, correlating with abnormal actin bundling in these processes (Figures 5G and 5H). This observation suggests that skipping of the hinge domain in FLNB may possibly increase FLNB's rigidity, thereby leading to more densely packed actin filaments. To determine whether such changes also impact FLNB's secondary functions in mechanosensation and cell motility,[28] previously implicated by our transcriptomic analyses (Figure 2F), we examined localization of a key mechanosensory protein-nesprin-2. Nesprin-2 is a core component of the LINC (Linker of nucleoskeleton and cytoskeleton) complex, anchoring actin filaments to the nuclear envelope and enabling force transmission and nuclear positioning during mechanotransduction. Immunostaining revealed a consistent reduction in nesprin-2 localization at the nuclear envelope in both C929 and C952 mutant iCNs compared to isogenic controls (Figures 5I and 5J), in line with recent observations in ALS patient neurons and tissue.[42] This reduction suggests weakening of the actin-nuclear envelope connection, providing a mechanistic link between altered *FLNB* splicing, impaired mechanotransduction and disrupted nuclear-cytoskeletal coupling in *C9orf72* mutant neurons.

DISCUSSION

ALS is a clinically and genetically heterogeneous neurodegenerative disease, marked by diverse presentations, progression rates and multiple cellular mechanisms.[43,44] This complexity hinders the identification of shared pathogenic pathways and the development of broadly effective therapies. The *C9orf72* HRE, the most common genetic cause, drives pathology through multiple mechanisms, including haploinsufficiency, toxic RNA foci, and DPR proteins.[2,3,6,7] While iPSC-derived neurons have revealed diverse cellular defects, reproducible transcriptomic insights remain limited due to challenges in inconsistent neuronal differentiation, lack of rigorous isogenic controls and insufficient sequencing depth. Global transcriptomic profiling offers a powerful approach to uncover convergent gene expression and splicing changes that may underlie *C9orf72* ALS.

To address these limitations, we performed deep RNA sequencing on iPSC-derived cortical neurons generated from two independent *C9orf72* patient lines and their respective isogenic controls. By using a transcription factor-driven differentiation approach, we generated homogeneous neuronal populations that minimized experimental variability across patient lines. Although NGN2-induced neuronal models can exhibit heterogeneity depending on the induction strategy, the use of a clonal, safe-harbor integrated NGN2 system in this study minimizes such heterogeneity, as supported by consistent lineage marker expression across biological replicates and across isogenic control and *C9orf72* mutant lines (Figure S5A). Furthermore, the stability of the *C9orf72* G4C2 repeat expansion during neuronal differentiation has been demonstrated in prior studies, including the original characterization of the iPSC lines used here, which showed that repeat length remains following differentiation into neurons while retaining RNA foci pathology.[16] Consistent with this, we observe robust RNA foci in NGN2-induced cortical neurons, supporting that the molecular phenotypes identified arise in neurons harboring a stable C9orf72 repeat expansion.

This controlled system enabled robust detection of gene expression and splicing alterations directly attributable to the *C9orf72* HRE. In parallel, we also identified consistent cellular phenotypes across multiple patient-derived iCNs, supporting the transcriptomic findings at a functional level. To our knowledge, this is the first study to combine high-depth transcriptomic analysis with reproducible cellular phenotyping across multiple isogenic *C9orf72* iPSC-derived neuron lines, providing a robust and scalable framework for uncovering shared early molecular mechanisms in *C9orf72* ALS.

Our study revealed consistent dysregulation of ALS-relevant pathways, particularly those involved in cytoskeletal organization, synaptic signaling and ECM adhesion, processes essential

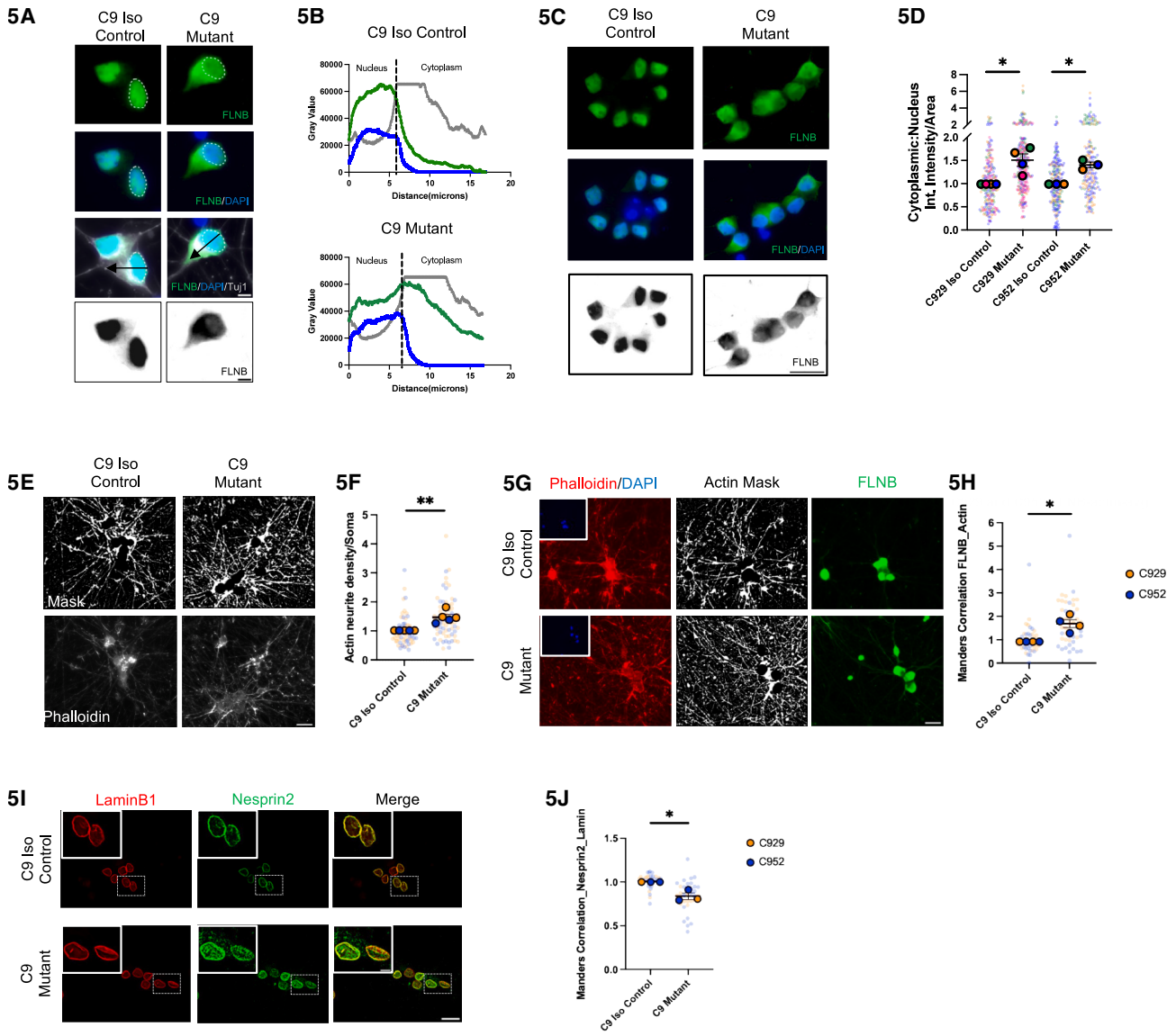

Figure 5. *C9orf72* mutant iCNs show FLNB nuclear clearance, altered actin organization and impaired mechanotransduction

(A and C) Immunofluorescence showing altered nuclear-cytoplasmic localization of FLNB in *C9orf72* mutant iCNs at DIV15. Scale bars, (A) 5 μm; (C) 20 μm.

(B) Line scan analysis of FLNB signal intensity relative to Tuj1 and DAPI staining.

(D) Graphs quantifying cytoplasmic-to-nuclear FLNB intensity per area in *C9orf72* Iso control and mutant iCNs (n = 3–4 biological replicates per line; ∼250–300 cells total).

(E) Representative images of phalloidin-stained neurites and actin density masks in Iso control and mutant iCNs. Scale bars, 20 μm.

(F) Graphs of actin density normalized to soma area (n = 2 [C952]–3 [C929] biological replicates; ∼60–70 fields of view [FOV] total).

(G) Immunofluorescence images showing FLNB and phalloidin co-staining. Actin mask denotes neurite regions analyzed. Scale bars, 20 μm.

(H) Super plot quantifying FLNB-actin colocalization (n = 2 biological replicates per line; ∼50 FOV total).

(I) Representative images showing altered LINC complex protein nesprin-2 in mutant iCNs at DIV15. Scale bars, full image = 20 μm, inset = 5 μm.

(J) Super plot quantifying nesprin-2 colocalization (n = 2 [C952], 1 [C929] biological replicates; ∼30 FOV total).

Data in (D, F, H, and J): large dots represent replicate means; small dots show individual cell values. Error bars indicate mean ± SEM. Statistical analysis by two-tailed unpaired t test with Welch's correction on replicate means. $p < 0.05$ (*), $p < 0.01$ (**), $p < 0.001$ (***), and $p < 0.0001$ (****).

for neuronal structure and function. Our study further uncovered a reproducible *FLNB* skipping in exon 30 across three of the patient iCN lines and the downstream cellular consequences with impaired nuclear-cytoplasmic transport, actin crosslinking and mechanosensory pathways (Figures 6A–6C). The findings reported here align in part with prior studies, including the AnswerALS dataset and single-cell RNA-seq of *C9orf72* patient iPSC-derived motor neurons, which reported ECM and adhesion gene alterations.[45] Our study builds upon these findings using a more rigorous isogenic system and RNA deep sequencing of

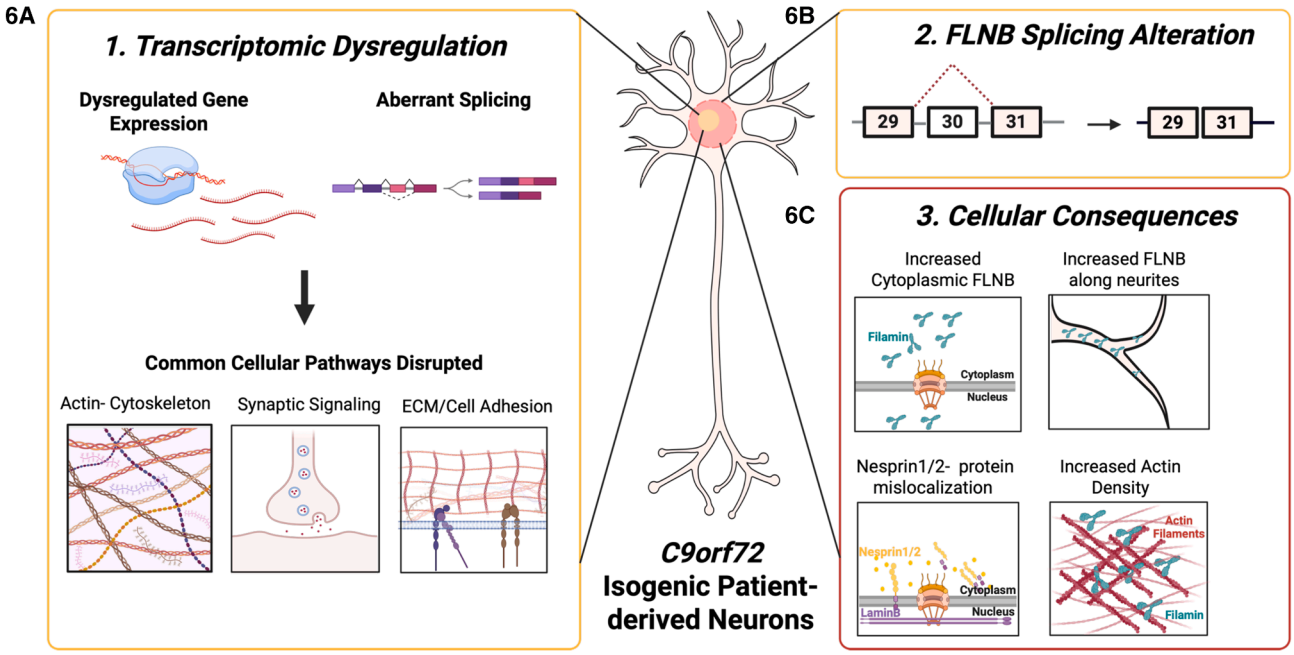

Figure 6. Summary of convergent transcriptomic and functional alterations in *C9orf72* iCNs

(A) Schematic summary of commonly dysregulated pathways identified in this study across multiple *C9orf72* patient-derived iCN lines.
(B) Illustration of *FLNB* exon 30 skipping in *C9orf72* mutant iCNs, potentially leading to (C) multiple cellular consequences in increased cytoplasmic accumulation of FLNB, altered actin density and dysregulation of mechanosensory gene and proteins.
Figure created in https://BioRender.com.

iPSC-derived cortical neurons, offering enhanced resolution into convergent molecular disruptions in *C9orf72* ALS. Several multi-omic studies across different subtypes of ALS have similarly highlighted changes in RNA splicing, axonal transport, synaptic signaling and ECM remodeling, further supporting the importance of these pathways across diverse ALS mutations.[46–48]

Notably, our analysis consistently identified dysregulation of *CTSF*, *TMOD1*, *RAB31*, and *PCDHA2* across multiple patient-derived iCN lines, with additional line-dependent changes observed for *DNAJA4*. These genes are linked to lysosomal function, actin regulation, stress responses, synaptic membrane trafficking, cell adhesion, and neurite outgrowth and their reproducible alteration suggests early, convergent molecular defects in *C9orf72* ALS.[49–54] Whether these changes drive pathogenesis or reflect compensatory mechanisms to mitigate the mutational burden remains to be determined through targeted gene manipulation studies. Supporting this, Milito et al. reported conserved ECM remodeling in polyGR/PR knock-in mouse models, pointing to early neuroprotective or maladaptive responses to repeat toxicity and previous work from our laboratory showed that modulation of actin-cytoskeleton can help rescue key ALS phenotypes in nuclear-cytoplasmic transport in *C9orf72* neurons.[55,56]

Among all genes analyzed, *CTSF*, a lysosomal protease, emerged as one of the most robustly upregulated gene across all *C9orf72* mutant iCN lines with increased CTSF protein accumulation within nuclei (Figures 2G-H, S2F, and S2G) further suggesting a potential functional consequence of this early transcriptomic shift. Although classical apoptotic markers such as cleaved caspase-3 were not elevated (Figures S2H and S2I), the consistent upregulation of CTSF may reflect an early stress-primed state, potentially predisposing neurons to apoptotic degeneration over time.

In addition to altered gene expression, our splicing analysis revealed significant dysregulation in genes involved in cytoskeletal organization, synaptic signaling and ECM adhesion, pathways also highlighted in the expression data. This suggests that splicing alterations contribute to disruptions in key neuronal functions. Although no individual genes were consistently altered at both expression and splicing levels across mutant iCNs, the convergence of affected pathways points to broader dysregulation at the network level.

To further examine the upstream mechanisms driving the widespread splicing abnormalities in *C9orf72* mutant iCNs, we employed rMAPS to look at splicing alterations with RBP motif enrichment and identify potential regulatory drivers. This analysis highlighted broad involvement of RBPs and identified SRSF1, FMR1, and HNRNPK among others as top candidates contributing to the observed splicing defects (Figure S3E). These RBPs are essential for RNA processing and have been previously implicated in neurodegenerative diseases, including ALS. Notably, SRSF1 is known to be sequestered by G4C2 repeat RNA foci, promoting nuclear export of toxic transcripts and facilitating RAN translation, both of which contribute to cellular toxicity.[57] Similarly, HNRNPK, a nuclear RBP, becomes mislocalized to the cytoplasm in *C9orf72* ALS cells, impairing its nuclear functions in DNA repair and RNA metabolism.[58] Such mis-localization in RBPs, rather than transcriptional downregulation, likely might represent a critical pathogenic mechanism in

C9orf72-associated disease. This cascade of dysfunction may underlie the transcriptomic instability observed in *C9orf72* ALS/FTD and contribute to early neuronal vulnerability.

A key splicing alteration detected was the neuron-specific skipping of exon 30 hinge domain in *FLNB*, critical for actin crosslinking flexibility, nuclear translocation and mechano-transduction.[25,29–34] Loss of this domain may promote a more rigid FLNB protein isoform, disrupting cytoskeletal dynamics, mechano-transduction and transcriptional regulation. Supporting this theory, we observed nuclear clearance and cytoplasmic accumulation of FLNB protein in *C9orf72* iCNs, along with disrupted actin crosslinking and impaired mechanosensory function. These changes parallel findings previous studies who showed that CRISPR-mediated exon 30 deletion of *FLNB* leads to nuclear exclusion of the protein, highlighting the possible hinge domain's role in nuclear localization.[37] This splicing alteration may also be a result of broader nuclear transport deficits in *C9orf72* mutant neurons, as suggested by altered Ran localization in our initial observations on this mutant line. Although total *FLNB* transcript levels were unchanged across patient lines, exon 30 skipping likely impairs both cytoskeletal flexibility and FLNB's transcriptional regulatory functions, contributing to neuronal dysfunction.

Similarly, *FLNB* exon 30 skipping has been observed in glioblastoma where the loss of the hinge domain promoted increased cell migration, a phenotype that can be linked to altered mechanosignaling functions.[59] These parallels suggest that *FLNB* splicing alterations may similarly contribute to neuronal vulnerability in *C9orf72* ALS by disrupting cytoskeletal remodeling and nuclear signaling. Although *FLNB* exon 30 skipping has been reported in glioma, the biological context of these findings differs substantially from the post-mitotic neuronal environment examined here. In contrast to highly proliferative, oncogenic systems, the consistent mutation-linked splicing change observed in our cortical-like neurons supports a C9orf72-dependent mechanism. In the context of the epithelial-mesenchymal transition in cancer cell lines, the work by Li et al. identified key upstream RBP regulators QKI and RBFOX1 mediating *FLNB* exon 30 alternative splicing.[37] While their findings provide a valuable framework, the mechanisms governing splicing are often highly context-dependent, and therefore, in our *C9orf72* iCNs, we did not observe significant changes in the expression of their candidate RBPs or a predicted enrichment of these RBPs motifs regulating splicing events. This suggests that a distinct set of regulatory factors could possibly drive the aberrant splicing of *FLNB* in the *C9orf72* neurodegenerative disease setting. Therefore, future unbiased studies employing techniques such as iCLIP in isogenic *C9orf72* iCNs will be critical for definitively mapping the RBP interactions at the *FLNB* locus and evaluating their potential as therapeutic targets to restore normal splicing. Furthermore, our study observed consistent *FLNB* exon 30 skipping across multiple patient *C9orf72* iCNs that were absent in control/patient derived fibroblasts, suggesting a disease relevant, neuron-specific change. This may reflect unique splicing mechanisms of cytoskeletal genes essential for post-mitotic cells, which are not present in proliferative somatic lineages.

Although we observe a reproducible alteration in FLNB intracellular localization in *C9orf72* mutant neurons, the present data do not distinguish whether this phenotype is driven directly by *FLNB* exon 30 skipping or by a broader nucleocytoplasmic transport defects associated with C9orf72 pathology, or by a combination of both mechanisms. Accordingly, we interpret the FLNB localization changes as correlative with the splicing alteration rather than as definitive evidence of causality.

Importantly, exon 30 encodes a short internal peptide within FLNB, and currently available antibodies do not allow isoform-specific detection of exon 30-containing versus Δexon30 FLNB at endogenous levels in human neurons. This technical limitation hinders the direct assessment of isoform-specific FLNB protein abundance or localization in the current study. Definitive mechanistic dissection will therefore require isoform-specific genetic and proteomic approaches, such as targeted expression or knock-in of FLNB Δexon30 and exon 30-containing FLNB, to directly test how this splicing event influences FLNB localization and function in neurons.

Furthermore, given the focus of this study on transcriptomic and splicing alterations in iPSC derived neurons, systematic analysis of C9orf72 protein changes across differentiation remains an important area for future work. Secondly, our study focuses on early post-mitotic NGN2-induced cortical neurons, we did not observe overt basal cell death under our culture conditions, suggesting that extended differentiation or stress-based paradigms may be required to uncover downstream effects on viability or autophagy defects. Lastly, our data identify *FLNB* exon 30 skipping as a robust, genotype-specific splicing alteration in *C9orf72* iPSC derived neurons, direct testing of how exon-specific *FLNB* isoforms influence neuronal viability, autophagy, and cytoskeletal dynamics will require isoform-specific genetic manipulation and represent an important direction for future work.

In conclusion, our study reveals conserved, early transcriptional and splicing abnormalities across patient isogenic *C9orf72* neuronal system. The identification of dysregulated genes involved in ECM adhesion, cytoskeletal organization, and synaptic signaling highlights early mechanisms of neuronal vulnerability and shows the utility of isogenic iPSC-derived neurons for uncovering convergent pathways. These findings lay a foundation for future biomarker development and therapeutic targeting in ALS.

Limitations of the study

While our study uncovers robust cell-autonomous transcriptomic and splicing alterations across multiple patient-derived isogenic *C9orf72* iCNs, several limitations should be acknowledged. First, analyses were performed at a single early time point (DIV15), limiting insight into the temporal progression of these molecular changes. Longitudinal studies are needed to determine whether early transcriptomic dysregulation contributes to downstream ALS hallmarks, such as axonal degeneration, survival defects or TDP-43 mislocalization. Second, our focus on cortical neurons leaves open the question of whether similar alterations occur in other vulnerable populations, including spinal motor neurons. Although we observed early transcriptomic and cellular changes in mutant iCNs, the direct link between these changes and neurodegeneration remains to be validated, extending the analysis to later time points may help address this.

Collectively, these limitations emphasize the need for integrative, multi-lineage models to more comprehensively capture ALS pathophysiology and enhance translational relevance.

RESOURCE AVAILABILITY

Lead contact

Further information and requests for resources and reagents should be directed to, and will be fulfilled by, the lead contact, John Landers (john.landers@umassmed.edu).

Materials availability

New cell lines and materials made during this study will be made available upon request to the lead contact, subject to the completion of a materials transfer agreement.

Data and code availability

- All raw FASTQ files and processed RNA-seq datasets generated in this study have been deposited in the Gene Expression Omnibus under accession number GSE303931. This accession number is also listed in the key resources table.
- The study does not report original computational code. All visualizations were generated using standard R packages.
- Any additional information required to reanalyze the data reported in this study is available from the lead contact upon request.

ACKNOWLEDGMENTS

We thank the Cedars-Sinai Medical Center's Stem Cell Core Laboratory for providing the CS29iALS-C9n1, ISO, CS52iALS-C9n6, and ISO iPSC lines. We thank Dr. Michael E. Ward for his generous gift of CLYBL1 targeting NGN2 cassette, Dr. Claudia Fallini for the generous gift of CS52iALS-C9n6 and CS52iALS-C9n6ISO NGN2 lines, and Dr. Jeffery Rothstein and Dr. Kevin Talbot for the OXC9 iPSC lines. We thank Drs. Zuoshang Xu, Daryl Bosco, Sandra Almeida, Gregory Pazour, and Jonathan Glass (Emory University) for their valuable feedback on the work. This work was supported by grants from the NIH (R61/33NS13060) to J.E.L. Figure 1A, 4B, and 6A-6C was created with BioRender.com.

AUTHOR CONTRIBUTIONS

Conceptualization, A.S., D.M.B., and J.E.L.; methodology, A.S., A.B., D.M.B., and J.E.L.; investigation and validation, A.S., A.B., D.M.B., K.S., and V.R.D.; formal analysis, A.S., A.B., D.M.B., K.S., V.R.D., and J.H.; software, A.S., A.B., and D.M.B.; visualization, A.S., A.B., D.M.B., and J.H.; writing – original draft, A.S., A.B., and D.M.B.; writing – review and editing, all authors; resources and funding acquisition, J.E.L.

DECLARATION OF INTERESTS

J.E.L. is a consultant for ACI Clinical LLC sponsored by Biogen, Inc. and Ionis Pharmaceuticals, Inc.

STAR★METHODS

Detailed methods are provided in the online version of this paper and include the following:

SUPPLEMENTAL INFORMATION

Supplementary data related to this article can be found online at https://doi.org/10.1016/j.isci.2026.116054.

Received: November 5, 2025
Revised: November 13, 2025
Accepted: May 5, 2026

REFERENCES

1. Brown, R.H., and Al-Chalabi, A. (2017). Amyotrophic Lateral Sclerosis. N. Engl. J. Med. *377*, 162–172. https://doi.org/10.1056/NEJMra1603471.
2. DeJesus-Hernandez, M., Mackenzie, I.R., Boeve, B.F., Boxer, A.L., Baker, M., Rutherford, N.J., Nicholson, A.M., Finch, N.A., Flynn, H., Adamson, J., et al. (2011). Expanded GGGGCC hexanucleotide repeat in noncoding region of C9ORF72 causes chromosome 9p-linked FTD and ALS. Neuron *72*, 245–256. https://doi.org/10.1016/j.neuron.2011.09.011.
3. Renton, A.E., Majounie, E., Waite, A., Simón-Sánchez, J., Rollinson, S., Gibbs, J.R., Schymick, J.C., Laaksovirta, H., van Swieten, J.C., Myllykangas, L., et al. (2011). A hexanucleotide repeat expansion in C9ORF72 is the cause of chromosome 9p21-linked ALS-FTD. Neuron *72*, 257–268. https://doi.org/10.1016/j.neuron.2011.09.010.
4. Majounie, E., Renton, A.E., Mok, K., Dopper, E.G.P., Waite, A., Rollinson, S., Chiò, A., Restagno, G., Nicolaou, N., Simon-Sanchez, J., et al. (2012). Frequency of the C9orf72 hexanucleotide repeat expansion in patients with amyotrophic lateral sclerosis and frontotemporal dementia: a cross-sectional study. Lancet Neurol. *11*, 323–330. https://doi.org/10.1016/S1474-4422(12)70043-1.
5. Marogianni, C., Rikos, D., Provatas, A., Dadouli, K., Ntellas, P., Tsitsi, P., Patrinos, G., Dardiotis, E., Hadjigeorgiou, G., and Xiromerisiou, G. (2019). The role of C9orf72 in neurodegenerative disorders: a systematic review, an updated meta-analysis, and the creation of an online database. Neurobiol. Aging *84*, 238.e25–238.e34. https://doi.org/10.1016/j.neurobiolaging.2019.04.012.
6. Balendra, R., and Isaacs, A.M. (2018). C9orf72-mediated ALS and FTD: multiple pathways to disease. Nat. Rev. Neurol. *14*, 544–558. https://doi.org/10.1038/s41582-018-0047-2.
7. Babić Leko, M., Župunski, V., Kirincich, J., Smilović, D., Hortobágyi, T., Hof, P.R., and Šimić, G. (2019). Molecular mechanisms of neurodegeneration related to c9orf72 hexanucleotide repeat expansion. Behav. Neurol. *2019*, 2909168. https://doi.org/10.1155/2019/2909168.
8. Gendron, T.F., Bieniek, K.F., Zhang, Y.-J., Jansen-West, K., Ash, P.E.A., Caulfield, T., Daughrity, L., Dunmore, J.H., Castanedes-Casey, M., Chew, J., et al. (2013). Antisense transcripts of the expanded C9ORF72 hexanucleotide repeat form nuclear RNA foci and undergo repeat-associated non-ATG translation in c9FTD/ALS. Acta Neuropathol. *126*, 829–844. https://doi.org/10.1007/s00401-013-1192-8.
9. Zu, T., Liu, Y., Bañez-Coronel, M., Reid, T., Pletnikova, O., Lewis, J., Miller, T.M., Harms, M.B., Falchook, A.E., Subramony, S.H., et al. (2013). RAN

proteins and RNA foci from antisense transcripts in C9ORF72 ALS and frontotemporal dementia. Proc Natl Acad Sci USA *110*, E4968–E4977. https://doi.org/10.1073/pnas.1315438110.

10. Sellier, C., Corcia, P., Vourc'h, P., and Dupuis, L. (2024). C9ORF72 hexanucleotide repeat expansion: From ALS and FTD to a broader pathogenic role? Rev. Neurol. *180*, 417–428. https://doi.org/10.1016/j.neurol.2024.03.008.
11. Zhang, K., Donnelly, C.J., Haeusler, A.R., Grima, J.C., Machamer, J.B., Steinwald, P., Daley, E.L., Miller, S.J., Cunningham, K.M., Vidensky, S., et al. (2015). The C9orf72 repeat expansion disrupts nucleocytoplasmic transport. Nature *525*, 56–61. https://doi.org/10.1038/nature14973.
12. Lagier-Tourenne, C., Baughn, M., Rigo, F., Sun, S., Liu, P., Li, H.-R., Jiang, J., Watt, A.T., Chun, S., Katz, M., et al. (2013). Targeted degradation of sense and antisense C9orf72 RNA foci as therapy for ALS and frontotemporal degeneration. Proc Natl Acad Sci USA *110*, E4530–E4539. https://doi.org/10.1073/pnas.1318835110.
13. Mori, K., Weng, S.-M., Arzberger, T., May, S., Rentzsch, K., Kremmer, E., Schmid, B., Kretzschmar, H.A., Cruts, M., Van Broeckhoven, C., et al. (2013). The C9orf72 GGGGCC repeat is translated into aggregating dipeptide-repeat proteins in FTLD/ALS. Science *339*, 1335–1338. https://doi.org/10.1126/science.1232927.
14. Haeusler, A.R., Donnelly, C.J., and Rothstein, J.D. (2016). The expanding biology of the C9orf72 nucleotide repeat expansion in neurodegenerative disease. Nat. Rev. Neurosci. *17*, 383–395. https://doi.org/10.1038/nrn.2016.38.
15. Fernandopulle, M.S., Prestil, R., Grunseich, C., Wang, C., Gan, L., and Ward, M.E. (2018). Transcription Factor-Mediated Differentiation of Human iPSCs into Neurons. Curr. Protoc. Cell Biol. *79*, e51. https://doi.org/10.1002/cpcb.51.
16. Sareen, D., O'Rourke, J.G., Meera, P., Muhammad, A.K.M.G., Grant, S., Simpkinson, M., Bell, S., Carmona, S., Ornelas, L., Sahabian, A., et al. (2013). Targeting RNA foci in iPSC-derived motor neurons from ALS patients with a C9ORF72 repeat expansion. Sci. Transl. Med. *5*, 208ra149. https://doi.org/10.1126/scitranslmed.3007529.
17. Ababneh, N.A., Scaber, J., Flynn, R., Douglas, A., Barbagallo, P., Candalija, A., Turner, M.R., Sims, D., Dafinca, R., Cowley, S.A., and Talbot, K. (2020). Correction of amyotrophic lateral sclerosis related phenotypes in induced pluripotent stem cell-derived motor neurons carrying a hexanucleotide expansion mutation in C9orf72 by CRISPR/Cas9 genome editing using homology-directed repair. Hum. Mol. Genet. *29*, 2200–2217. https://doi.org/10.1093/hmg/ddaa106.
18. Mizielinska, S., Lashley, T., Norona, F.E., Clayton, E.L., Ridler, C.E., Fratta, P., and Isaacs, A.M. (2013). C9orf72 frontotemporal lobar degeneration is characterised by frequent neuronal sense and antisense RNA foci. Acta Neuropathol. *126*, 845–857. https://doi.org/10.1007/s00401-013-1200-z.
19. Shi, Y., Lin, S., Staats, K.A., Li, Y., Chang, W.-H., Hung, S.-T., Hendricks, E., Linares, G.R., Wang, Y., Son, E.Y., et al. (2018). Haploinsufficiency leads to neurodegeneration in C9ORF72 ALS/FTD human induced motor neurons. Nat. Med. *24*, 313–325. https://doi.org/10.1038/nm.4490.
20. Selvaraj, B.T., Livesey, M.R., Zhao, C., Gregory, J.M., James, O.T., Cleary, E.M., Chouhan, A.K., Gane, A.B., Perkins, E.M., Dando, O., et al. (2018). C9ORF72 repeat expansion causes vulnerability of motor neurons to Ca2+-permeable AMPA receptor-mediated excitotoxicity. Nat. Commun. *9*, 347. https://doi.org/10.1038/s41467-017-02729-0.
21. Donnelly, C.J., Zhang, P.-W., Pham, J.T., Haeusler, A.R., Mistry, N.A., Vidensky, S., Daley, E.L., Poth, E.M., Hoover, B., Fines, D.M., et al. (2013). RNA toxicity from the ALS/FTD C9ORF72 expansion is mitigated by antisense intervention. Neuron *80*, 415–428. https://doi.org/10.1016/j.neuron.2013.10.015.
22. Lee, Y.-B., Chen, H.-J., Peres, J.N., Gomez-Deza, J., Attig, J., Stalekar, M., Troakes, C., Nishimura, A.L., Scotter, E.L., Vance, C., et al. (2013). Hexanucleotide repeats in ALS/FTD form length-dependent RNA foci, sequester RNA binding proteins, and are neurotoxic. Cell Rep. *5*, 1178–1186. https://doi.org/10.1016/j.celrep.2013.10.049.
23. Shen, S., Park, J.W., Lu, Z.x., Lin, L., Henry, M.D., Wu, Y.N., Zhou, Q., and Xing, Y. (2014). rMATS: robust and flexible detection of differential alternative splicing from replicate RNA-Seq data. Proc Natl Acad Sci USA *111*, E5593–E5601. https://doi.org/10.1073/pnas.1419161111.
24. Hwang, J.Y., Jung, S., Kook, T.L., Rouchka, E.C., Bok, J., and Park, J.W. (2020). rMAPS2: an update of the RNA map analysis and plotting server for alternative splicing regulation. Nucleic Acids Res. *48*, W300–W306. https://doi.org/10.1093/nar/gkaa237.
25. Nakamura, F., Stossel, T.P., and Hartwig, J.H. (2011). The filamins: organizers of cell structure and function. Cell Adhes. Migrat. *5*, 160–169.
26. Sutherland-Smith, A.J. (2011). Filamin structure, function and mechanics: are altered filamin-mediated force responses associated with human disease? Biophys. Rev. *3*, 15–23. https://doi.org/10.1007/s12551-011-0042-y.
27. van der Flier, A., Kuikman, I., Kramer, D., Geerts, D., Kreft, M., Takafuta, T., Shapiro, S.S., and Sonnenberg, A. (2002). Different splice variants of filamin-B affect myogenesis, subcellular distribution, and determine binding to integrin [beta] subunits. J. Cell Biol. *156*, 361–376. https://doi.org/10.1083/jcb.200103037.
28. Feng, Y., and Walsh, C.A. (2004). The many faces of filamin: a versatile molecular scaffold for cell motility and signalling. Nat. Cell Biol. *6*, 1034–1038. https://doi.org/10.1038/ncb1104-1034.
29. Razinia, Z., Mäkelä, T., Ylänne, J., and Calderwood, D.A. (2012). Filamins in mechanosensing and signaling. Annu. Rev. Biophys. *41*, 227–246. https://doi.org/10.1146/annurev-biophys-050511-102252.
30. van der Flier, A., and Sonnenberg, A. (2001). Structural and functional aspects of filamins. Biochim. Biophys. Acta *1538*, 99–117. https://doi.org/10.1016/s0167-4889(01)00072-6.
31. Zhou, A.-X., Hartwig, J.H., and Akyürek, L.M. (2010). Filamins in cell signaling, transcription and organ development. Trends Cell Biol. *20*, 113–123. https://doi.org/10.1016/j.tcb.2009.12.001.
32. Ma, H.-R., Cao, L., Wang, F., Cheng, C., Jiang, R., Zhou, H., Xie, Z., Wuermanbieke, S., and Qian, Z. (2020). Filamin B extensively regulates transcription and alternative splicing, and is associated with apoptosis in HeLa cells. Oncol. Rep. *43*, 1536–1546. https://doi.org/10.3892/or.2020.7532.
33. Hu, J., Lu, J., Lian, G., Ferland, R.J., Dettenhofer, M., and Sheen, V.L. (2014). Formin 1 and filamin B physically interact to coordinate chondrocyte proliferation and differentiation in the growth plate. Hum. Mol. Genet. *23*, 4663–4673. https://doi.org/10.1093/hmg/ddu186.
34. Sheen, V.L., Feng, Y., Graham, D., Takafuta, T., Shapiro, S.S., and Walsh, C.A. (2002). Filamin A and Filamin B are co-expressed within neurons during periods of neuronal migration and can physically interact. Hum. Mol. Genet. *11*, 2845–2854. https://doi.org/10.1093/hmg/11.23.2845.
35. Di Donato, M., Bilancio, A., D'Amato, L., Claudiani, P., Oliviero, M.A., Barone, M.V., Auricchio, A., Appella, E., Migliaccio, A., Auricchio, F., and Castoria, G. (2015). Cross-talk between androgen receptor/filamin A and TrkA regulates neurite outgrowth in PC12 cells. Mol. Biol. Cell *26*, 2858–2872. https://doi.org/10.1091/mbc.E14-09-1352.
36. Gardel, M.L., Nakamura, F., Hartwig, J.H., Crocker, J.C., Stossel, T.P., and Weitz, D.A. (2006). Prestressed F-actin networks cross-linked by hinged filamins replicate mechanical properties of cells. Proc Natl Acad Sci USA *103*, 1762–1767. https://doi.org/10.1073/pnas.0504777103.
37. Li, J., Choi, P.S., Chaffer, C.L., Labella, K., Hwang, J.H., Giacomelli, A.O., Kim, J.W., Ilic, N., Doench, J.G., Ly, S.H., et al. (2018). An alternative splicing switch in FLNB promotes the mesenchymal cell state in human breast cancer. eLife *7*, e37184. https://doi.org/10.7554/eLife.37184.
38. Zhang, J., Ito, H., Wate, R., Ohnishi, S., Nakano, S., and Kusaka, H. (2006). Altered distributions of nucleocytoplasmic transport-related proteins in the spinal cord of a mouse model of amyotrophic lateral sclerosis. Acta Neuropathol. *112*, 673–680. https://doi.org/10.1007/s00401-006-0130-4.
39. McGoldrick, P., Lau, A., You, Z., Durcan, T.M., and Robertson, J. (2023). Loss of C9orf72 perturbs the Ran-GTPase gradient and nucleocytoplasmic

transport, generating compositionally diverse Importin β-1 granules. Cell Rep. *42*, 112134. https://doi.org/10.1016/j.celrep.2023.112134.

40. Zhang, K., Daigle, J.G., Cunningham, K.M., Coyne, A.N., Ruan, K., Grima, J.C., Bowen, K.E., Wadhwa, H., Yang, P., Rigo, F., et al. (2018). Stress granule assembly disrupts nucleocytoplasmic transport. Cell *173*, 958–971.e17. https://doi.org/10.1016/j.cell.2018.03.025.
41. Beckers, J., Tharkeshwar, A.K., Fumagalli, L., Contardo, M., Van Schoor, E., Fazal, R., Thal, D.R., Chandran, S., Mancuso, R., Van Den Bosch, L., and Van Damme, P. (2023). A toxic gain-of-function mechanism in C9orf72 ALS impairs the autophagy-lysosome pathway in neurons. Acta Neuropathol. Commun. *11*, 151. https://doi.org/10.1186/s40478-023-01648-0.
42. Sirtori, R., J Gregoire, M., M Potts, E., Collins, A., Donatelli, L., and Fallini, C. (2024). LINC complex alterations are a key feature of sporadic and familial ALS/FTD. Acta Neuropathol. Commun. *12*, 69. https://doi.org/10.1186/s40478-024-01778-z.
43. Tzeplaeff, L., Wilfling, S., Requardt, M.V., and Herdick, M. (2023). Current state and future directions in the therapy of ALS. Cells *12*, 1523. https://doi.org/10.3390/cells12111523.
44. Mejzini, R., Flynn, L.L., Pitout, I.L., Fletcher, S., Wilton, S.D., and Akkari, P.A. (2019). ALS genetics, mechanisms, and therapeutics: where are we now? Front. Neurosci. *13*, 1310. https://doi.org/10.3389/fnins.2019.01310.
45. Ho, R., Workman, M.J., Mathkar, P., Wu, K., Kim, K.J., O'Rourke, J.G., Kellogg, M., Montel, V., Banuelos, M.G., Arogundade, O.A., et al. (2021). Cross-Comparison of Human iPSC Motor Neuron Models of Familial and Sporadic ALS Reveals Early and Convergent Transcriptomic Disease Signatures. Cell Syst. *12*, 159–175.e9. https://doi.org/10.1016/j.cels.2020.10.010.
46. Ye, L., Dittlau, K.S., Sicart, A., Janky, R., Van Damme, P., and Van Den Bosch, L. (2025). Sporadic ALS hiPSC-derived motor neurons show axonal defects linked to altered axon guidance pathways. Neurobiol. Dis. *206*, 106815. https://doi.org/10.1016/j.nbd.2025.106815.
47. Held, A., Adler, M., Marques, C., Reyes, C.J., Kavuturu, A.S., Quadros, A.R.A.A., Ndayambaje, I.S., Lara, E., Ward, M., Lagier-Tourenne, C., and Wainger, B.J. (2023). iPSC motor neurons, but not other derived cell types, capture gene expression changes in postmortem sporadic ALS motor neurons. Cell Rep. *42*, 113046. https://doi.org/10.1016/j.celrep.2023.113046.
48. Workman, M.J., Lim, R.G., Wu, J., Frank, A., Ornelas, L., Panther, L., Galvez, E., Perez, D., Meepe, I., Lei, S., et al. (2023). Large-scale differentiation of iPSC-derived motor neurons from ALS and control subjects. Neuron *111*, 1191–1204.e5. https://doi.org/10.1016/j.neuron.2023.01.010.
49. Wang, B., Shi, G.P., Yao, P.M., Li, Z., Chapman, H.A., and Brömme, D. (1998). Human cathepsin F. Molecular cloning, functional expression, tissue localization, and enzymatic characterization. J. Biol. Chem. *273*, 32000–32008. https://doi.org/10.1074/jbc.273.48.32000.
50. Yamashiro, S., Gokhin, D.S., Sui, Z., Bergeron, S.E., Rubenstein, P.A., and Fowler, V.M. (2014). Differential actin-regulatory activities of Tropomodulin1 and Tropomodulin3 with diverse tropomyosin and actin isoforms. J. Biol. Chem. *289*, 11616–11629. https://doi.org/10.1074/jbc.M114.555128.
51. Zarouchlioti, C., Parfitt, D.A., Li, W., Gittings, L.M., and Cheetham, M.E. (2018). DNAJ Proteins in neurodegeneration: essential and protective factors. Philos. Trans. R. Soc. Lond. B Biol. Sci. *373*, 20160534. https://doi.org/10.1098/rstb.2016.0534.
52. Chua, C.E.L., and Tang, B.L. (2014). Engagement of the small GTPase Rab31 protein and its effector, early endosome antigen 1, is important for trafficking of the ligand-bound epidermal growth factor receptor from the early to the late endosome. J. Biol. Chem. *289*, 12375–12389. https://doi.org/10.1074/jbc.M114.548321.
53. Shao, Z., Noh, H., Bin Kim, W., Ni, P., Nguyen, C., Cote, S.E., Noyes, E., Zhao, J., Parsons, T., Park, J.M., et al. (2019). Dysregulated protocadherin-pathway activity as an intrinsic defect in induced pluripotent stem cell-derived cortical interneurons from subjects with schizophrenia. Nat. Neurosci. *22*, 229–242. https://doi.org/10.1038/s41593-018-0313-z.
54. Chen, W.V., and Maniatis, T. (2013). Clustered protocadherins. Development *140*, 3297–3302. https://doi.org/10.1242/dev.090621.
55. Milioto, C., Carcolé, M., Giblin, A., Coneys, R., Attrebi, O., Ahmed, M., Harris, S.S., Lee, B.I., Yang, M., Ellingford, R.A., et al. (2024). PolyGR and polyPR knock-in mice reveal a conserved neuroprotective extracellular matrix signature in C9orf72 ALS/FTD neurons. Nat. Neurosci. *27*, 643–655. https://doi.org/10.1038/s41593-024-01589-4.
56. Giampetruzzi, A., Danielson, E.W., Gumina, V., Jeon, M., Boopathy, S., Brown, R.H., Ratti, A., Landers, J.E., and Fallini, C. (2019). Modulation of actin polymerization affects nucleocytoplasmic transport in multiple forms of amyotrophic lateral sclerosis. Nat. Commun. *10*, 3827. https://doi.org/10.1038/s41467-019-11837-y.
57. Rossi, S., Serrano, A., Gerbino, V., Giorgi, A., Di Francesco, L., Nencini, M., Bozzo, F., Schininà, M.E., Bagni, C., Cestra, G., et al. (2015). Nuclear accumulation of mRNAs underlies G4C2-repeat-induced translational repression in a cellular model of C9orf72 ALS. J. Cell Sci. *128*, 1787–1799. https://doi.org/10.1242/jcs.165332.
58. Braems, E., Bercier, V., Van Schoor, E., Heeren, K., Beckers, J., Fumagalli, L., Dedeene, L., Moisse, M., Geudens, I., Hersmus, N., et al. (2022). HNRNPK alleviates RNA toxicity by counteracting DNA damage in C9orf72 ALS. Acta Neuropathol. *144*, 465–488. https://doi.org/10.1007/s00401-022-02471-y.
59. Seong, M., Bak-Gordon, P., Liu, Z., Canoll, P.D., and Manley, J.L. (2025). Splicing dysregulation in glioblastoma alters the function of cell migration-related genes. Glia *73*, 251–270. https://doi.org/10.1002/glia.24630.
60. Baron, D.M., Fenton, A.R., Saez-Atienzar, S., Giampetruzzi, A., Sreeram, A., Danielson, E.W., Keagle, P.J., Keagle, P.J., Doocy, V.R., Smith, N.J., et al. (2022). ALS-associated KIF5A mutations abolish autoinhibition resulting in a toxic gain of function. Cell Rep. *39*, 110598. https://doi.org/10.1016/j.celrep.2022.110598.
61. Patro, R., Duggal, G., Love, M.I., Irizarry, R.A., and Kingsford, C. (2017). Salmon provides fast and bias-aware quantification of transcript expression. Nat. Methods *14*, 417–419. https://doi.org/10.1038/nmeth.4197.
62. Love, M.I., Huber, W., and Anders, S. (2014). Moderated estimation of fold change and dispersion for RNA-seq data with DESeq2. Genome Biol. *15*, 550. https://doi.org/10.1186/s13059-014-0550-8.
63. Vaquero-Garcia, J., Aicher, J.K., Jewell, S., Gazzara, M.R., Radens, C.M., Jha, A., Norton, S.S., Lahens, N.F., Grant, G.R., and Barash, Y. (2023). RNA splicing analysis using heterogeneous and large RNA-seq datasets. Nat. Commun. *14*, 1230. https://doi.org/10.1038/s41467-023-36585-y.
64. Zhou, Y., Zhou, B., Pache, L., Chang, M., Khodabakhshi, A.H., Tanaseichuk, O., Benner, C., and Chanda, S.K. (2019). Metascape provides a biologist-oriented resource for the analysis of systems-level datasets. Nat. Commun. *10*, 1523. https://doi.org/10.1038/s41467-019-09234-6.
65. Almeida, S., Gascon, E., Tran, H., Chou, H.J., Gendron, T.F., Degroot, S., Tapper, A.R., Sellier, C., Charlet-Berguerand, N., Karydas, A., et al. (2013). Modeling key pathological features of frontotemporal dementia with C9ORF72 repeat expansion in iPSC-derived human neurons. Acta Neuropathol. *126*, 385–399. https://doi.org/10.1007/s00401-013-1149-y.
66. Stirling, D.R., Swain-Bowden, M.J., Lucas, A.M., Carpenter, A.E., Cimini, B.A., and Goodman, A. (2021). CellProfiler 4: improvements in speed, utility and usability. BMC Bioinf. *22*, 433. https://doi.org/10.1186/s12859-021-04344-9.
67. Schindelin, J., Arganda-Carreras, I., Frise, E., Kaynig, V., Longair, M., Pietzsch, T., Preibisch, S., Rueden, C., Saalfeld, S., Schmid, B., et al. (2012). Fiji: an open-source platform for biological-image analysis. Nat. Methods *9*, 676–682. https://doi.org/10.1038/nmeth.2019.

STAR★METHODS

KEY RESOURCES TABLE

REAGENT or RESOURCE	SOURCE	IDENTIFIER
Antibodies		
Human/Mouse/Rat Sox2 Antibody (Clone #245610)	R&D Systems	Cat# MAB2018; RRID: AB_3657808
Human Oct4 Antibody	R&D Systems	Cat# MAB17591; RRID: AB_10719296
Chicken anti-βIII-Tubulin	Aves Labs	Cat # TUJ; RRID: AB_2313564
MAP2 Polyclonal Antibody	ProteinTech	Cat# 17490-1-AP; RRID: AB_2137880
Mouse anti-Tau1	Millipore	Cat#MAB3420; RRID: AB_3068606
Rabbit anti-VGLUT1	ProteinTech	Cat# 55491-1-AP; RRID: AB_2881348
Mouse anti-FLNB	Thermo Fisher Scientific	MA527748; RRID: AB_2735183
Mouse anti-Nesprin-2	Millipore	Cat# MABC86
Rabbit anti-Lamin B1	ProteinTech	Cat# 12987-1-AP; RRID: AB_2136290
Mouse anti-cleaved Caspase-3	Cell Signaling Technology	Cat# 9661T; RRID: AB_2341188
Anti-GAPDH Antibody	Novus Biologicals	Cat# NB300-327; RRID: AB_10077604
Anti-Tubulin Beta 3 (TUBB3) Antibody-Cy5 conjugated	BioLegend	Cat# 657406; RRID: AB_2563610
Rabbit Anti-RAN Antibody	Bethyl Laboratories	Cat# A304-297A; RRID: AB_2620172
Donkey Anti-Mouse 488	Jackson Immunoresearch	Cat# 715-545-150; RRID: AB_2340846
Donkey Anti-Rabbit IgG 594	Invitrogen	Cat# A-21207; RRID: AB_141637
Donkey Anti-Mouse 546	Invitrogen	Cat# A10036; RRID: AB_2534012
Goat Anti-Rabbit 488	Invitrogen	Cat# A11008; RRID: AB_143165
Rabbit Anti-TDP-43	ProteinTech	Cat# 10782-2-AP; RRID: AB_615042
Mouse Anti-Cathepsin F	R&D Systems	Cat# MAB2075; RRID: AB_2087381
Biological samples		
CS29iALS-C9n1 (C929 mutant iPSC)	Cedars-Sinai Biomanufacturing Core	Cat# CS29iALS-C9n1; RRID: CVCL_W559
CS29iALS-C9n1.ISOT2RB4 (C929 isogenic control iPSC)	Cedars-Sinai Biomanufacturing Core	CS Vial ID: 984944, 984945
CS52iALS-C9n1 (C952 mutant iPSC)	Cedars-Sinai Biomanufacturing Core	Cat# CS52iALS-C9n1; RRID: CVCL_W561
CS52iALS-C9n6.ISOC3 (C952 control)	Cedars-Sinai Biomanufacturing Core	CS Vial ID: 964782, 964783
OXC9 mutant iPSC lines	Gift from Dr. Kevin Talbot	Ababneh et al.[17]
OXC9 control iPSC lines	Gift from Dr. Kevin Talbot	Ababneh et al.[17]
NGN2 engineered iPSC lines	This study	See Methods
Chemicals, peptides, and recombinant proteins		
RNase A, DNase and protease-free (10 mg/mL)	Thermo Fisher Scientific	Cat# EN0531
7-Deaza-2′-deoxyguanosine 5′-triphosphate lithium salt- (7-deaza-dGTP)	Sigma-Aldrich	Cat# D8783
2′-deoxyadenosine 5′-triphosphate 100 mM (dATP)	Invitrogen	Cat# 10216018
2′-deoxycytidine 5′-triphosphate 100 mM (dCTP)	Invitrogen	Cat# 10217016
2′-deoxythymidine 5′-triphosphate 100 mM (dTTP)	Invitrogen	Cat# 10219012
ProLong Gold Antifade Mountant with DAPI	Thermo Fisher Scientific	Cat# P36941
0.05% Trypsin EDTA	Gibco	Cat# 25300054
2-Mercaptoethanol, 99% pure	Fisher Scientific	Cat# AC125470100
Dulbecco's Modified Eagle Medium (DMEM)	Gibco	Cat# 11965118
Fetal Bovine Serum, Tet System Approved	Takara	Cat# 631101
Heat-Inactivated Fetal Bovine Serum Corning Cat# MT35011CV	–	–

(*Continued on next page*)

Continued

REAGENT or RESOURCE	SOURCE	IDENTIFIER
L-glutamine (200 mM)	Gibco	Cat# 25030081
Penicillin/Streptomycin	Gibco	Cat# 15140122
BSA (heat shock fraction, protease free)	Sigma-Aldrich	Cat# A3294
Triton X-100	Sigma-Aldrich	Cat# T9284
Prolong Gold Antifade Mountant with DAPI	Invitrogen	Cat# P-36931
Blasticidin S Hydrochloride Powder	Research Products International	Cat# B12200
Ultrapure DNase/RNase-Free Distilled Water	Invitrogen	Cat# 10977015
Laemmli SDS-Sample Buffer	Boston BioProducts	Cat# BP-111R
Dulbecco's Phosphate Buffered Saline	Corning	Cat# 20-031-CV
Tween 20	Fisher BioReagents	Cat# BP337-500
Trypsin-EDTA	Gibco	Cat# 15400054
Odyssey Blocking Buffer	Licor	Cat# 927-40010
Dulbecco's Modified Eagle Medium	Sigma-Aldrich	Cat# D7777
BrainPhys Neuronal Culture Medium	STEMCELL Technologies	Cat# 05790
Formaldehyde	Fisher	Cat# BP531-500
Matrigel hESC-Qualified Matrix	Corning	Cat# 08-774-552
ROCK Inhibitor	Selleck Chemicals	Cat# S1049
Lipofectamine Stem Transfection Reagent	Invitrogen	Cat# STEM00001
Stemflex Medium	Gibco	Cat# A3349401
Poly-L-Ornithine	Sigma	Cat# P3655 (3000–7000 kDa)
Laminin	Invitrogen	Cat# 23017-015
Natural Mouse Laminin	Corning	Cat# 354232
B27 Supplement	Gibco	Cat# 17504044
Non-essential amino acids (NEAA), 100×	Gibco	Cat# 17502048
Doxycycline	Sigma	Cat# D9891
Glutamax 200 mM	Invitrogen	Cat# 35050-061
N2 Supplement	Gibco	Cat# 17502048
BDNF	PeproTech	Cat# 450-02
NT-3	PeproTech	Cat# 450-03
B27 Plus Neuronal Culture System	Gibco	Cat# A3653401
4–20% Mini-PROTEAN TGXTM Gel, 15 well, 15 μL	Bio-Rad	Cat# 456-1096
Nitrocellulose membrane/filter paper pack, pkg of 50	Bio-Rad	Cat# 1620213
Protease inhibitor tables	Roche	Cat# 11873580001
Critical commercial assays		
iScript cDNA Synthesis Kit	Bio-Rad	1708891
TaqMan Fast Advanced Master Mix	Thermo Fisher Scientific	4444556
ddPCR Supermix for Probes (No dUTP)	Bio-Rad	1863023
AccuPrime GC-Rich DNA Polymerase	Invitrogen	12337016
Q5 High-Fidelity DNA Polymerase	New England Biolabs	M0491
Pierce BCA Protein Assay Kit	ThermoFisher Scientific	Cat# 23227
TaqMan Gene Expression Assay Hs02786624_g1, GAPDH	Thermo Fisher Scientific	Assay ID: Hs02786624_g1
TaqMan Gene Expression Assay Hs00199313_m1, Rab31	Thermo Fisher Scientific	Assay ID: Hs00199313_m1
TaqMan Gene Expression Assay Hs00268513_m1, TMOD1	Thermo Fisher Scientific	Assay ID: Hs00268513_m1
TaqMan Gene Expression Assay Hs00388055_m1, DNAJA4	Thermo Fisher Scientific	Assay ID: Hs00388055_m1
TaqMan Gene Expression Assay Hs00258848_s1, PCDHA2	Thermo Fisher Scientific	Assay ID: Hs00258848_s1
TaqMan Gene Expression Assay Hs00186901_m1, CTSF	Thermo Fisher Scientific	Assay ID: Hs00186901_m1

(*Continued on next page*)

Continued

REAGENT or RESOURCE	SOURCE	IDENTIFIER
Deposited data		
Sequence data, analysis and resources related to the RNA sequencing of C929, C952 and isogenic control iCNs	This study	GEO: GSE303931
Experimental models: Cell lines		
Human fibroblast cell line AG11726	Coriell Institute for Medical Research	Cat# AG11726
Human fibroblast cell line AG08046	Coriell Institute for Medical Research	Cat# AG08046
Human fibroblast cell line GM03440	Coriell Institute for Medical Research	Cat# GM03440
Human fibroblast cell line AG12588	Coriell Institute for Medical Research	Cat# AG12588
Human fibroblast cell line C9036	Gift from Dr. Jonathan Glass	N/A
Human fibroblast cell line C9019	Gift from Dr. Jonathan Glass	N/A
Human fibroblast cell line C9041	Gift from Dr. Jonathan Glass	N/A
Human fibroblast cell line C9034	Gift from Dr. Jonathan Glass	N/A
Oligonucleotides		
sgRNA targeting CYBL locus - ATGTTGGAAGGATGAGGAAA	Fernandopulle et al. 2018[15]	N/A
C9orf72 RP-PCR forward primer- TGTAAAACGACGGCCAGTCAAGG AGGGAAACAACCGCAGCC	De Jesus Hernandez et al. 2011[22]	N/A
C9orf72 RP-PCR reverse primer- CAGGAAACAGCTATGACCGGGCCCGCCC CGACCACGCCCCGGCCCCGGCCCCGG	De Jesus Hernandez et al. 2011[22]	N/A
C9orf72 RP-PCR M13 anchor primer- CAGGAAACAGCTATGACC	De Jesus Hernandez et al. 2011[22]	N/A
FLNB RT-PCR forward primer	This study	ATCGCCTCCACTGTGAAAAC
FLNB RT-PCR reverse primer	This study	CCGTTCATGTCACTCACTGG
20× FLNB FAM-labeled (spliced) probe	Bio-Rad	Forward: TCGGTGGTGTTGATATTCCT; Reverse: TTCATGTCACTCACTGGGAC; Probe: TTCACTGTCATGGTGACCG AAGAGG; Fluorophore: FAM
20× FLNB HEX-labeled (unspliced) probe	Bio-Rad	Forward: TCGGTGGTGTTGATATTCCT; Reverse: TTCATGTCACTCACTGGGAC; Probe: GAGGAGGCACCGTAAATGCATG; Fluorophore: HEX
RNA FISH probe (GGCCCC)4	IDT	Custom
RNA FISH probe (CAGG)6	IDT	Custom
Recombinant DNA		
NGN2 cassette targeting CLYBL locus	Gift from Dr. Michael Ward	N/A
Software and algorithms		
Terra workflow platform	Broad Institute	https://terra.bio
STAR aligner	Dobin et al. 2013	https://github.com/alexdobin/STAR
Picard toolkit	Broad Institute	https://broadinstitute.github.io/picard
DESeq2	Love et al. 2014	https://bioconductor.org
rMATS version 4.0.2 http://rnaseq-mats.sourceforge.net/	Shen et al. 2014	http://rnaseq-mats.sourceforge.net
MAJIQ v2	Vaquero-Garcia et al. 2016	https://majiq.biociphers.org
rMAPS2	Hwang et al. 2020	http://rmaps.cecsresearch.org/
Metascape	Zhou et al. 2019	https://metascape.org

(*Continued on next page*)

Continued

REAGENT or RESOURCE	SOURCE	IDENTIFIER
IGV v2.19.1	Broad Institute	https://software.broadinstitute.org/software/igv
CellProfiler v4.2.8	Broad Institute	https://cellprofiler.org
ImageJ v2.14.0	NIH	https://imagej.nih.gov/ij
GraphPad Prism v9	GraphPad Software	https://graphpad.com
Biorender	Biorender	https://www.biorender.com
QuantaSoft software	Bio-Rad	N/A
Other		
NanoDrop spectrophotometer	Thermo Fisher Scientific	Cat# ND-1000
Agilent Bioanalyzer	Agilent Technologies	Cat# 2100 Bioanalyzer
NovaSeq 6000 Sequencer	Illumina	NovaSeq 6000
Nikon Ti Eclipse	Nikon	Ti Eclipse
Leica DMI6000 Leica Microsystems	Widefield Microscope	Cat# DMI6000
CFX 384 Real-Time PCR Detection System	BioRad	https://www.bio-rad.com/en-us/product/cfx384-touch-real-time-pcr-detectionsystem?ID=LJB22YE8Z
QX200 Droplet Digital PCR System	Bio-Rad	Cat# 1864001
QX600 AutoDG Droplet Digital PCR System	Bio-Rad	Cat# 17008371
QX600 Droplet Reader	Bio-Rad	Cat# 12013328

EXPERIMENTAL MODELS AND SUBJECT DETAILS

iPSC line information

The iPSC isogenic lines used in this study were obtained from Cedars Sinai Biomanufacturing Core (CS29iALS-C9n1- C929 Mutant, CS29iALS-C9n1.ISO2RB4- C929 Iso Control and CS52iALS-C9n1-C952 Mutant, CS52iALS-C9n6.ISOC3-C952 Iso Control. The OXC9 Iso Control and Mutant lines were a kind gift from Dr. Kevin Talbot.[17]

Additional fibroblast lines were obtained from Coriell Institute for Medical Research or gifted as described in the Key Resources Table. All cell lines were maintained under standard sterile conditions at 37°C and 5% CO_2 in appropriate growth media. All iPSC lines were authenticated by provider or previously published reports. Routine mycoplasma testing was not performed during this study, however all cell lines were maintained under standard sterile culture conditions.

Generation and characterization of *C9orf72* NGN2 iPSC lines

The CLYBL1-targeting NGN2 cassette, modified to include a blasticidin resistance marker (a kind gift from Dr. Michael Ward), was originally based on the construct described.[15] NGN2 line generation was performed following the protocol previously described for NIL iPSC lines.[60] Briefly, iPSCs were plated and transfected with the NGN2 cassette as outlined and resulting NGN2 iPSC lines were verified using immunofluorescence staining (protocol below) for pluripotency markers Oct4 and Sox2. All iPSC lines used were confirmed to have a normal karyotype (Quest Diagnostics) prior to and after inserting the NGN2 cassette.

iPSC culture and cortical neuronal differentiation

iPSCs were maintained and differentiated into cortical neurons using a previously described NGN2 induction protocol[15] with some modifications. Following NGN2 induction, cells were replated in induction media at a lower density (~52,000 cells/cm^2) than described. The following day, media was replaced with BrainPhys cortical neuron media (StemCell Technologies 05790), and the BrdU incubation period in media was extended to 72 h to enhance maturation. iCN medium was prepared using the BrainPhys Neuronal Culture System components and refreshed every 2–3 days using half-media changes until the experimental endpoint.

Fibroblasts culturing

C9orf72 and control fibroblasts were maintained at 37°C in a humidified incubator with 5% CO_2 in Dulbecco's Modified Eagle Medium (DMEM Invitrogen 11-965-092), supplemented with 15% (v/v) heat-inactivated fetal bovine serum (FBS MediaTech 35-010-CV), 2 mM L-glutamine (Gibco 25030081), 1% sodium pyruvate (Thermo Fisher 11360070), 1% (v/v) penicillin-streptomycin solution (Gibco 15140122). Biological replicates were derived from sequential passages for independent lines. Fibroblasts were harvested

72 h post-splitting and total RNA was extracted using the Qiagen RNeasy Mini Kit (Qiagen 74104) following the manufacturer's instructions. cDNA was synthesized from 1000 ng of total RNA using the iScript cDNA Synthesis Kit (Bio-Rad 1708891). FLNB transcript analysis was performed by RT-PCR as described below.

METHOD DETAILS

Repeat primed PCR

Genomic DNA was isolated from iPSCs grown in 6-well plates using a non-Chelex lysis and precipitation protocol. Briefly, cells were lysed, proteins were precipitated and removed, and DNA was recovered by isopropanol precipitation, washed, and resuspended in TE hydration buffer. DNA was incubated at 65 °C for 1 h, followed by overnight incubation at room temperature with gentle shaking and stored at −20 °C until use. Repeat-primed PCR was performed using *AccuPrime GC-Rich DNA Polymerase* (Invitrogen 12337016) and 300 ng of genomic DNA. Primer sequences were adapted from DeJesus-Hernandez et al.[2]

FAM-labeled forward primer: 5′-CAAGGAGGGAAACAACCGCAGCC-3′,

Reverse primer: 5′-GGGCCCGCCCCGACCACGCCCCGGCCCCGGCCCCGG-3′, Reverse M13 anchor primer: 5′-caggaaacagct atgacc-3'.

Each 25 μL reaction contained 1× GC-Rich buffer A, primers (final concentration of forward and reverse anchor at 1.4 μM, reverse primer at 0.7 μM), 0.5 μL polymerase, 300 ng DNA, and a 5 mM dNTP mix supplemented with 7-deaza-dGTP. The dNTP mix (final 5 mM) was prepared from 10 mM 7-deaza-dGTP (Sigma Aldrich D8783) and 100 mM dATP, dCTP, and dTTP stocks (Invitrogen 10216018, 10219012, 10217016). Thermal cycling was performed as follows: initial denaturation at 98 °C for 10 min; 10 cycles of 97 °C for 35 s, 64 °C for 2 min, and 68 °C for 8 min; followed by 25 cycles of 97 °C for 35 s, 64 °C for 2 min, and 68 °C for 8 min with a 20 s extension added per cycle. Ramp rates were adjusted to 0.5 °C/s (64% for denaturation/extension, 25% for annealing). PCR products were analyzed by capillary electrophoresis at the MGH DNA Core.

RNA sequencing

Total RNA was extracted from iCNs using the Qiagen RNeasy Mini Kit (Qiagen 74104), following the manufacturer's protocol. RNA concentration was assessed via a NanoDrop spectrophotometer and RNA integrity was determined by the UMMS Molecular Biology Core Labs (MBCL, UMass Medical School) using an Agilent Bioanalyzer. Only high-quality RNA samples with an RNA Integrity Number (RIN) $\geq$ 9.5 were used for library preparation. RNA libraries were generated using a poly((1) mRNA-seq library preparation protocol and sequenced on an Illumina NovaSeq 6000 platform to generate 2 × 150 bp paired-end reads, targeting a depth of ~100 million reads per sample. Sequencing was performed with n = 3 biological replicates/line at the Yale Center for Genome Analysis.

Differential gene expression and splicing bioinformatic analysis

Raw RNA-seq data were processed using Terra workflows (Broad Institute). Transcript-level quantification was performed with Salmon V0.11.3 (quant.genes files), and alignment-based processing was carried out with STAR against the human reference genome (GRCh38) to generate BAM files.[61] BAMs were sorted and indexed with Samtools, and quality control metrics (alignment statistics, mapping rate, duplication rate) were assessed using Picard toolkit, Broad Institute (https://gatk.broadinstitute.org/hc/en-us).

Differential gene expression analysis was conducted using the DESeq2 package,[62] with Wald tests applied to compare control and mutant lines. P-values were adjusted by the Benjamini-Hochberg method and genes were considered significant with P-adj<0.05, $|Log_2FC|$ >0.35. All plots and heatmaps were generated in RStudio (2023.12.0) and Terra-Galaxy, respectively. Overlap analysis was performed by combining significant gene lists (P-adj<0.05, $|Log_2FC|$ >0.(35) from each line and filtering for shared genes.

Alternative splicing events were identified using rMATS, including skipped exons (SEs), alternative 5′ splice sites (A5SS), alternative 3′ splice sites (A3SS), mutually exclusive exons (MXEs), and retained introns (RI).[23] The JCEC (Junction Counts and Exon Counts) output was used, which incorporates both junction-spanning and exon-mapping reads. Significant events were defined as those with an absolute change in percent spliced-in (FDR<0.15; $|\Delta PSI| \geq 0.2$). Sashimi plots were generated in the Integrative Genomics Viewer (IGV V2.19.1, Broad Institute) with default parameters. For FLNB, exon-junction reads quantifying percent skipped and unskipped transcripts were obtained from MAJIQ (V2) analysis.[63]

RNA-binding protein motif enrichment was analyzed using RMAPS2 (http://rmaps.cecsresearch.org) with combined FASTQ files from C929 and C952 control and mutant lines.[24] Genes meeting significance ($|\Delta PSI| \geq 0.2$; P-value <0.05) were used as input. Pathway enrichment analyses were performed using Metascape.[64]

RNA FISH

RNA FISH was performed as previously described in Almeida et al. 2013 with slight modifications. Briefly, after fixation in 4% paraformaldehyde, cells were treated with RNase A (40 μg/mL; Thermo Scientific EN0531) for 20 min at room temperature, washed in 1× PBS and permeabilized overnight in 70% ethanol at 4 °C. Hybridization was carried out using Cy3-conjugated $(GGCCCC)_4$ or $(CAGG)_6$ probes (IDT) at a final concentration of 65 nM in hybridization buffer, and incubated overnight at 37 °C in a humidified chamber. Post-hybridization washes were performed as described previously.[65] Coverslips were mounted in ProLong Gold Antifade with DAPI (Thermo Fisher Scientific P-(36941) and imaged the following day.

qPCR analysis

Total RNA was isolated from DIV15 iCNs using the Qiagen RNAeasy Mini Kit (Qiagen 74104). RNA was reverse transcribed using the iScript cDNA synthesis kit (Bio-Rad 1708891). Quantitative real-time PCR was performed in the Bio Rad CFX384 Real Time System with C1000 Touch Thermal Cycler using the TaqMan Fast Advanced Master Mix (ThermoFisher (4444556) and TaqMan Gene Expression Assay KITS (FAM, Hs02786624_g1, Hs00186901_m1, Hs00199313_m1, Hs00268513_m1, Hs00388055_m1, Hs00258848_s1) as per manufacturer's instructions. For relative expression, ΔΔCq method was employed, using GAPDH as an internal control. For each differentiation, quantitative RT-PCR was measured in triplicate and the mean for each differentiation used for analysis. An unpaired two-tailed *t* test followed by Welch's correction was used to determine significance.

RT-PCR analysis

Total RNA was isolated from DIV15 iCNs using the Qiagen RNeasy Mini Kit (74104) following the manufacturer's protocol. Reverse transcription was performed using the iScript cDNA Synthesis Kit (Bio-Rad 1708891) to generate cDNA from 500 ng or 1000 ng of total RNA per reaction. RT-PCR was performed on an Applied Biosystems Veriti PCR thermocycler using Q5 High-Fidelity DNA Polymerase (NEB). The PCR reactions were prepared as 50 μL reactions containing 1× Q5 reaction buffer (NEB), 200 μM dNTPs (NEB), 0.5 μM forward and reverse FLNB-specific primers (Forward: ATCGCCTCCACTGTGAAAAC, Reverse: CCGTTCATGTCACTCAC TGG), 0.04 U/μL Q5 polymerase (NEB) and 25 ng of cDNA. The thermal cycling protocol consisted of an initial denaturation at 98°C for 30 s, followed by 30 cycles of 98 °C for 10 s, 55 °C for 30 s and 72 °C for 10 s, with a final extension at 72 °C for 2 min and a hold at 4 °C. PCR products were resolved on a 2% agarose gel prepared in 1× TBE buffer. A total of 20 μL of PCR product mixed with 5 μL of gel loading dye was loaded per lane. Gels were run at 100 V for 15 min followed by 150 V for 30 min and imaged using the ImageLab System (Bio-Rad).

ddPCR analysis

Total RNA was isolated from DIV15 iCNs using the Qiagen RNeasy Mini Kit (Qiagen 74104) according to the manufacturer's instructions. Reverse transcription was performed using the iScript cDNA Synthesis Kit (Bio-Rad 1708891), generating cDNA from 500 ng or 1000 ng of total RNA per reaction. Droplet digital PCR (ddPCR) was conducted using Bio-Rad ddPCR reagents and instrumentation Briefly, ddPCR reactions were prepared in a final volume of 22 μL containing 1× ddPCR Supermix for Probes (No dUTP, Bio-Rad, Cat# 1863023), 20× FLNB exon 30 FAM-labeled (spliced) probe (Bio-rad, Forward sequence: TCGGTGGTGTTGATATT CCT, Reverse sequence: TTCATGTCACTCACTGG GAC, Probe Sequence: TTCACTGTCATGGTGA CCGAAGAGG), 20× FLNB exon 30 HEX-labeled (unspliced) probe (Bio-rad, Forward sequence: TCGGTGGTGTTGATATT CCT, Reverse sequence: TTCATGTCACTCA CTGG GAC, Probe Sequence: GAGGAGGCACCGGTA AATGCATG, Fluorophore: HEX) and 25 ng of cDNA, following the manufacturer's protocol. Droplets were generated either manually using DG8 cartridges (Bio-Rad 1864008) or via the QX600 Automated Droplet Generator (Biorad AutoDG) as per manufacturer's instructions. PCR amplification was performed on an Applied Biosystems Veriti thermocycler with the following thermal profile: 95 °C for 10 min (enzyme activation), followed by 40 cycles of 94 °C for 30 s (denaturation) and 60 °C for 1 min (annealing/extension) with a ramp rate of 2 °C/s, then 98 °C for 10 min (enzyme deactivation) and a final hold at 4 °C. After thermal cycling, droplets were read using a QX200 or QX600 Droplet Reader (Bio-Rad). Data were analyzed using Bio-Rad QuantaSoft software and the ratio of spliced (FAM+) to unspliced (HEX+) FLNB transcript was calculated for each condition, and the results were plotted as a stack bar plots with PSI calculated as Inclusion reads/(Inclusion+Exclusion reads). A two-tailed ANOVA test followed by Sidak multiple comparisons was used to determine significance.

Immunofluorescence

Immunofluorescence staining of iPSC lines and iPSC-derived iCNs were performed as previously described.[60] For iPSC marker staining, mouse anti-SOX2 (1:1000, R&D Systems MAB2018) and mouse anti-OCT4 (1:1000, R&D Systems MAB17591) were used. For iCN stainings, the following primary antibodies were used: chicken anti-βIII-Tubulin (1:300, Aves Labs AB_2313564), rabbit anti-MAP2 (1:250, ProteinTech 17490-1-AP), mouse anti-Tau1 (1:500, EMD Millipore MAB3420), rabbit anti-VGLUT1 (1:500, ProteinTech 55491-1-AP), mouse anti-FLNB (1:300, ThermoFisher MA5-27748), mouse anti-Nesprin-2 (1:300, Millipore MABC86), rabbit anti-Lamin B1 (1:400, ProteinTech 12987-1-AP), rabbit anti-TDP-43 (1:250, ProteinTech 10782-2-AP) and mouse anti-CTSF (1:250, R and D Systems MAB2075-SP). Host species matched secondary antibodies (Jackson ImmunoResearch) were diluted 1:1000 in PBSAT and incubated for 1 h at RT. Where indicated, Cy5-conjugated Tuj1 (1:500, BioLegend 657406) was applied directly to iCNs for 1 h following secondary antibody incubations.

Western blotting

Western blot analyses were performed as previously reported.[60] Primary antibodies were used as follows: 1:1000 for mouse anti-cleaved caspases 3 (CST 9661T), 1:1000 rabbit anti-GAPDH (Novus NB300-327). Blots were visualized with an Odyssey Infrared Imager (LiCor Model 9120).

Image analysis using CellProfiler and ImageJ

Cells were imaged using a Nikon Ti-E widefield microscope equipped with a 100× objective and an Andor Zyla cooled CMOS camera, using a 320 nm excitation source. Z-stacks were acquired at 0.3 μm intervals across the full cell volume. Image analysis were performed using CellProfiler (V4.2.(8) and ImageJ (V2.14.0)[66,67]

Nuclear-cytoplasmic localization analysis

Sum intensity projections of FLNB stained images were generated for image analysis using ImageJ (V2.14.0). Nuclear and cytoplasmic regions were defined using DAPI and Tuj1 staining, respectively. Line scans were performed by drawing parallel lines across DAPI and Tuj1 channels, and gray intensity values along the lines were measured using ImageJ to visualize nuclear versus cytoplasmic signal distribution.

For compartment-specific quantification, image analysis was performed in CellProfiler (V4.2.(8) using a custom pipeline. Nuclei (DAPI) and cell bodies (Tuj1) were segmented with the IdentifyPrimaryObjects and IdentifySecondaryObjects modules. FLNB signal intensity was measured in each compartment using the MeasureIntensity module, and compartment areas were used to calculate mean integrated intensity per area. A cytoplasmic-to-nuclear FLNB intensity ratio was computed for each cell. Mean ratios were averaged across biological replicates (n = 3–4), and statistical significance was assessed using an unpaired two-tailed *t* test with Welch's correction on replicate means. Similar analysis was performed for CTSF/TDP-43/Ran localization using respective nuclei (DAPI) and cell bodies (Tuj1) compartments.

Neurite (actin) density quantifications

Maximum intensity projections of Phalloidin stained images were generated for analysis using ImageJ (V2.14.0). Neurite density was quantified using CellProfiler (V4.2.(8) pipeline. Thresholded Phalloidin staining was used to segment neurites, with DAPI used to identify individual cell nuclei. A composite neurite network mask was generated by combining high- and low-intensity phalloidin signals and neurite area was measured. Soma area was obtained by enlarging DAPI nuclei area for each cell. Neurite density was normalized to soma area across each image, and mean area values were calculated per biological replicate. Statistical significance was assessed using an unpaired two-tailed *t* test with Welch's correction on replicate means.

Colocalization analysis

FLNB, DAPI, and Phalloidin (actin) channels were thresholded using the IdentifyPrimaryObjects module in CellProfiler. Colocalization between FLNB and Phalloidin was assessed using the Colocalization module to calculate Manders' correlation coefficients for each image. Mean values per biological replicate were plotted, and statistical significance was determined using an unpaired two-tailed *t* test with Welch's correction. For Nesprin-2 and LaminB, images were deconvolved prior to generating sum intensity projections. Colocalization analysis was then performed and Manders' coefficients were computed for each image.

QUANTIFICATION AND STATISTICAL ANALYSIS

All statistical analyses were performed using GraphPad Prism (v9; GraphPad Software, San Diego, CA). Unless otherwise noted in the figure legends, comparisons were made using unpaired two-tailed t-tests. The number of biological replicates is reported in the corresponding figure legends. Significance thresholds are indicated as follows: $p < 0.05$ (*), $p < 0.01$ (**), $p < 0.001$ (***), and $p < 0.0001$ (****).